

Subsonic turbulence in smoothed particle hydrodynamics and moving-mesh simulations

Andreas Bauer^{1*} and Volker Springel^{1,2}

¹*Heidelberger Institut für Theoretische Studien, Schloss-Wolfsbrunnengasse 35, 69118 Heidelberg, Germany*

²*Zentrum für Astronomie der Universität Heidelberg, Astronomisches Recheninstitut, Mönchhofstr. 12-14, 69120 Heidelberg, Germany*

23 August 2021

ABSTRACT

Highly supersonic, compressible turbulence is thought to be of tantamount importance for star formation processes in the interstellar medium (ISM). Likewise, cosmic structure formation is expected to give rise to subsonic turbulence in the intergalactic medium (IGM), which may substantially modify the thermodynamic structure of gas in virialized dark matter halos and affect small-scale mixing processes in the gas. Numerical simulations have played a key role in characterizing the properties of astrophysical turbulence, but thus far systematic code comparisons have been restricted to the supersonic regime, leaving it unclear whether subsonic turbulence is faithfully represented by the numerical techniques commonly employed in astrophysics. Here we focus on comparing the accuracy of smoothed particle hydrodynamics (SPH) and our new moving-mesh technique AREPO in simulations of driven subsonic turbulence. To make contact with previous results, we also analyze simulations of transsonic and highly supersonic turbulence. We find that the widely employed standard formulation of SPH yields problematic results in the subsonic regime. Instead of building up a Kolmogorov-like turbulent cascade, large-scale eddies are quickly damped close to the driving scale and decay into small-scale velocity noise. Reduced viscosity settings improve the situation, but the shape of the dissipation range differs compared with expectations for a Kolmogorov cascade. In contrast, our moving-mesh technique does yield power-law scaling laws for the power spectra of velocity, vorticity and density, consistent with expectations for fully developed isotropic turbulence. We show that large errors in SPH's gradient estimate and the associated subsonic velocity noise are ultimately responsible for producing inaccurate results in the subsonic regime. In contrast, SPH's performance is much better for supersonic turbulence, as here the flow is kinetically dominated and characterized by a network of strong shocks, which can be adequately captured with SPH. When compared to fixed-grid Eulerian simulations of turbulence, our moving-mesh approach shows qualitatively very similar results, although with somewhat better resolving power at the same number of cells, thanks to reduced advection errors and the automatic adaptivity of the AREPO code.

Key words: hydrodynamics, shock waves, turbulence, methods: numerical

1 INTRODUCTION

Astrophysical gas dynamics in the interstellar and intergalactic medium is typically characterized by very high Reynolds numbers, thanks to the comparatively low gas densities encountered in these environments, which imply a very low physical viscosity for the involved gas. We may hence expect that turbulent cascades over large dynamic ranges are rather prevalent, provided effective driving processes exist. Such turbulence can then be an important feature of gas dynamics, for example providing an additional effective

pressure contribution, or leading to thorough small-scale mixing of chemical elements in the gas.

In fact, it is believed that turbulence in the interstellar medium (ISM) plays a key role in the formation of ordinary stellar populations, determining in part the initial mass function of stars, the lifetime of molecular clouds, and the overall efficiency of star formation (e.g. Klessen et al. 2000; Mac Low & Klessen 2004). Here the turbulence is highly supersonic, and presumably driven primarily by supernova explosions. In addition, the strong radiative cooling processes of the ISM make its equation-of-state approximately isothermal, such that very strong shocks and high compression ratios are associated with the supersonic gas motions. An additional complexity arises from magnetic fields that are flux-frozen into the

* E-mail: andreas.bauer@h-its.org

gas, such that the relevant behaviour is that of isothermal, driven, supersonic, magnetohydrodynamic turbulence.

Another regime where turbulence is thought to be important lies in cosmological structure formation, particularly in virialized gaseous halos, and in mildly non-linear filaments. Here small-scale random motions may contribute a significant fraction of the pressure support in group- and cluster-sized halos. For example, Schuecker et al. (2004) analysed pressure fluctuations in the Coma cluster, finding them to be well described by a Kolmogorov power spectrum with a lower limit of 10% of the total ICM pressure being in turbulent form. Besides this direct observational evidence, there are also strong analytic arguments that suggest that hierarchical mergers should be able to generate and sustain subsonic turbulence in galaxy clusters (Subramanian et al. 2006).

Turbulence in the intracluster (ICM) and intergalactic medium (IGM) is expected to be primarily of subsonic character, allowing it to be approximately described as incompressible turbulence. The linear growth of structure driven by gravity is not expected to be able to generate this turbulence directly, due to the irrotational character of the gravitational force field. However, during non-linear structure formation, curved accretion and flow shocks can introduce vorticity into the gas. Also, the baroclinic term in the wake of mergers can act as an efficient source of vorticity, providing a large-scale driving of intrahalo turbulence. Already a moderate degree of gas turbulence may then have important consequences for the thermodynamic structure of quasi hydrostatic halos. For example, turbulence may help to create entropy cores in clusters (Mitchell et al. 2009; ZuHone 2011), and its dissipation provides for thermal heating. Also, the transport and the mixing of metals is affected by turbulent gas motions. All of these effects can modify the radiative cooling rates of intrahalo plasma, which immediately impacts galaxy formation at the halo centers (Vogelsberger et al. 2011). In addition, turbulence can be expected to influence the magnetic field structure in virialized halo gas, which in turn affects transport processes in the plasma such as thermal conduction (e.g. Parrish et al. 2012) or physical viscosity (Sijacki & Springel 2006).

A considerable difficulty for the understanding of turbulence lies in the comparatively limited quantitative knowledge that could thus far be gained from purely analytic considerations. While Kolmogorov's theory for the scaling laws of self-similar, incompressible turbulence still stands out as one of the most insightful characterizations of the physics of turbulence, an assessment of the accuracy of theories for turbulence, especially when constructed for particularly challenging cases such as compressible magnetohydrodynamic turbulence, has relied to a large extent on numerical simulations. Most simulations of astrophysical flows solve the Euler equations and not the Navier-Stokes equations, based on the realization that the residual physical viscosity is overwhelmed by numerical viscosity anyway at the achievable resolutions. The dynamic range per dimension that can be realized in 3D turbulence simulations is indeed quite small, rarely exceeding a factor 10^3 at present. Thus only a small inertial range and comparatively low Reynolds numbers can be resolved directly. Nevertheless, numerous numerical studies of the properties of astrophysical turbulence have been carried out and have already led to significant advances in our understanding of this important phenomenon.

This is especially true for the study of highly supersonic turbulence relevant for star formation, where a large body of literature has been accumulated, including systematic comparisons of different numerical techniques (Mac Low et al. 1998; Kitsionas et al. 2009; Kritsuk et al. 2011). For example, Kitsionas et al. (2009) have compared different hydrodynamical codes (4 mesh codes and

3 SPH codes) when applied to the decay of supersonic turbulence. They found generally somewhat higher dissipation rates in SPH (which can however be modified with different artificial viscosity parameterizations), but concluded that on scales resolved with at least 32 resolution elements per dimension, results were found to be qualitatively similar, at least as far as the decay of the Mach number with time was concerned. The velocity power spectra, however, revealed that the damping on smaller scales was consistently larger in SPH than in the grid codes.

In contrast, Price & Federrath (2010) claimed excellent agreement for driven supersonic Mach $\mathcal{M} = 10$ turbulence between the SPH-code PHANTOM and the Eulerian mesh-code FLASH. In particular, they found a consistent Kolmogorov-like slope in the power spectrum of the variable $\rho^{1/3}v$. Their plain velocity power spectra also agreed over an extended range of wave number k at large scales, although the SPH result eventually dipped down earlier. In the density power spectrum on the other hand, their SPH result yielded more power at high k , which can be interpreted as a welcome result of the adaptive resolution of SPH. Price & Federrath (2010) also argued that previous claims of a steeper slope for the turbulence spectrum in SPH by Padoan et al. (2007), based on simulations presented by Ballesteros-Paredes et al. (2006), may have been a resolution effect only.

While the agreement reported by Price & Federrath (2010) for SPH and mesh codes is encouraging, it is important to keep in mind that this was achieved for highly supersonic turbulence. The very different physics of such a flow compared with subsonic turbulence should caution against taking it for granted that this reassuring success carries over to subsonic flow as well. In particular, we note that Padoan et al. (2007) observed that there appears to be a Mach number dependence of the turbulent slope in SPH, where for $\mathcal{M} = 3$ a slightly steeper (and hence 'more wrong') slope was obtained than for $\mathcal{M} = 6$. This may mean that one tends to get a more accurate result with SPH when the Mach number is high. Indeed, in a response paper to our study, Price (2012) pointed out that for higher Mach number one naturally expects a higher Reynolds number in SPH for given viscosity settings, which should then also allow a larger inertial range.

In order to clarify these issues further, we focus in this paper on the topic of subsonic turbulence, which is thought to be important in cosmological structure formation. For example, Ryu et al. (2008) propose that vorticity generation along large-scale structure formation shocks creates significant turbulence outside filaments, and plays an important role in the production of intergalactic magnetic fields in clusters, groups and filaments. Dolag et al. (2005) and Vazza et al. (2006) used SPH to study turbulence in galaxy clusters formed in cosmological simulations. They found evidence for scaling laws where the total turbulent energy in the ICM scales with cluster mass. Lau et al. (2009) argued that the effective pressure associated with ICM turbulence may introduce a bias in the cluster masses inferred from hydrostatic models. Dolag et al. (2005) introduced and tested a scheme for reduced viscosity in SPH, finding that this produces significantly higher levels of turbulent gas motions than for ordinary viscosity, reaching up to 5-30% of the thermal energy. In this study, they also measured a turbulent power spectrum for the central 500 kpc of a simulated cluster, finding a significantly shallower slope than expected for Kolmogorov turbulence.

Similar results were obtained by Valdarnini (2011), who has presented the most detailed study of cluster turbulence based on SPH thus far, including an investigation of the impact of artificial viscosity on the results. The study finds that a Kolmogorov-like

$\mathcal{M} \sim 0.3$ turbulence simulations				
	resolution elements			
	64 ³	128 ³	256 ³	512 ³
SPH	S1	S2	S3	S4
SPH (time dependent AV)	S1-tav	S2-tav	S3-tav	
AREPO (moving-mesh)	A1	A2	A3	A4
Fixed Cartesian grid	F1	F2	F3	F4

Table 1. Names of primary simulation runs for $\mathcal{M} \sim 0.3$ turbulence. We consider calculations with three different numerical methods, (1) SPH with default parameters as implemented in the GADGET code and with a time dependent artificial viscosity parameterization, (2) the moving-mesh approach of AREPO, and (3) a fixed Cartesian mesh, which is also realized with AREPO.

$\mathcal{M} \sim 0.3$ turbulence, variants of SPH simulations		
Run name	resolution	Characteristics
S2-ngb1	128 ³	$N_{\text{ngb}} = 180$ smoothing neighbours
S2-ngb2	128 ³	$N_{\text{ngb}} = 512$ smoothing neighbours
S3- $\alpha = 0.1$	256 ³	reduced viscosity coefficient $\alpha = 0.1$
S3- $\alpha = 0.01$	256 ³	reduced viscosity coefficient $\alpha = 0.01$
S3- $\alpha = 0.001$	256 ³	reduced viscosity coefficient $\alpha = 0.001$
S3- $\alpha = 0.0001$	256 ³	reduced viscosity coefficient $\alpha = 0.0001$
S3-balsara	256 ³	enabled Balsara shear viscosity factor
S3-tav-balsara	256 ³	TAV + Balsara shear viscosity factor

Table 2. Variations of the numerical parameters of our standard SPH simulation for driven $\mathcal{M} \sim 0.3$ turbulence. For resolutions of 128³ or 256³, we carry out several simulations where either the number of SPH smoothing neighbours, or the artificial viscosity parameterization is changed, as indicated in the table.

slope for the longitudinal velocity spectrum can be reached for a limited range of wave numbers, but the solenoidal power spectrum appears to be rather strongly affected by numerical resolution effects (in fact, the measured slopes are much steeper than Kolmogorov for all viscosity schemes, and this was found to be robust as a function of resolution over the tested range). Overall, Valdarnini (2011) finds that turbulent motions account for a few to 10% of the thermal energy content.

Mesh-based studies of cluster turbulence find similar or even higher contributions of the kinetic energy in turbulence relative to the thermal energy in the ICM (Iapichino & Niemeyer 2008; Vazza et al. 2009; Maier et al. 2009; Lau et al. 2009; Vazza et al. 2011; Paul et al. 2011; Schmidt & Federrath 2011; Iapichino et al. 2011; Jones et al. 2011). For example, Vazza et al. (2011) report 5 to 30% based on simulations with the ENZO code. All these studies agree that major mergers efficiently inject turbulence, and produce a radial trend where the importance of turbulence increases with radial distance. In particular, Paul et al. (2011) point out that there is a close connection between turbulence production and virialization. Also, they show that the turbulence after a major merger is quite long-lived, still accounting for about 15% of the thermal energy after 4 Gyrs and 5% after 10 Gyrs. Zhu et al. (2010, 2011) have examined turbulence and vorticity in the intergalactic medium, claiming that at $z = 0$ the IGM is in a fully turbulent state on scales less than about ~ 3 Mpc and that this significantly modifies structure formation and the gas fractions in low mass halos.

Unlike in the case of supersonic turbulence, there is a paucity of systematic examinations of the accuracy of different numerical

Mach number	$\mathcal{M} \sim 1.2$	$\mathcal{M} \sim 3.5$	$\mathcal{M} \sim 8.4$
SPH	S3-m1	S3-m5	S3-m10
AREPO (moving-mesh)	A3-m1	A3-m5	A3-m10
Fixed Cartesian grid	F3-m1	F3-m5	F3-m10

Table 3. Simulations carried out for transsonic and supersonic driven turbulence. For the three Mach numbers examined here, $\mathcal{M} \sim 1.2$, $\mathcal{M} \sim 3.5$ and $\mathcal{M} \sim 8.4$, we carry out simulations at a fixed nominal resolution of 256³ particles/cells with three different methods, SPH, a moving mesh, and a fixed Cartesian mesh.

	$\mathcal{M} \sim 0.3$	$\mathcal{M} \sim 1.2 - 3.5$	$\mathcal{M} \sim 8.4$
σ	0.014	0.21 / 3.0	12.247
Δt	0.005	0.005	0.005
t_s	1	0.5	0.05
k_{min}	6.27	6.27	6.27
k_{max}	12.57	12.57	18.85
$k \propto$	$k^{-5/3}$	$k^{-5/3}$	$-(k - k_c)^2$

Table 4. Summary of the parameters of the turbulent driving routine used in our simulations.

techniques for representing subsonic turbulence. Only a few studies have considered subsonic turbulence in SPH thus far (Violeau & Issa 2007; Monaghan 2011; Robinson & Monaghan 2011) and we are not aware of a comparative analysis of three-dimensional simulations in this regime. However, an examination of this question is particularly timely because serious differences between Eulerian mesh-codes and SPH have been reported in a number of recent papers (e.g. Agertz et al. 2007). Given also that numerical differences in the representation of turbulence have been suspected to significantly influence cooling rates of halos and therefore impact galaxy formation (Vogelsberger et al. 2011; Sijacki et al. 2011; Keres et al. 2011), it is important to address this gap in detail.

In this study, we therefore compare the behaviour of turbulence simulations with three different numerical methods. We use the smoothed particle hydrodynamics implementation of the widely employed GADGET code and compare it with the novel AREPO technique (Springel 2010), both using a moving mesh or a fixed Cartesian mesh. We primarily focus on the poorly studied subsonic regime, but we also perform some simulations of transsonic and supersonic turbulence to be able to compare our results with the recent literature, and to characterize the behaviour of our new AREPO code in this regime as well. In this paper, we will only examine the well established “standard formulation” of SPH (as described, for example, in Springel & Hernquist 2002), supplemented also with a time dependent artificial viscosity parameterization. We note however that a number of recent works proposed extensions or modifications of classic SPH that aim to improve the accuracy of this method (e.g. Wadsley et al. 2008; Price 2008; Heß & Springel 2010; Read et al. 2010; Read & Hayfield 2011; Abel 2011). Our results do not necessarily extend to these new flavours of SPH, and it remains to be seen whether they can resolve the problems pointed out here.

This paper is organized as follows. In Section 2, we outline our numerical techniques and describe our simulation set, as well as our analysis techniques. In Section 3, we present our results for simulations in the subsonic regime. We then turn to results for the transsonic and supersonic regimes in Section 4. Finally, we give a discussion of our findings and present our conclusions in Section 5.

2 METHODOLOGY

2.1 Numerical methods

2.1.1 Moving- and fixed-mesh simulations with AREPO

AREPO implements a novel quasi-Lagrangian scheme for solving the Euler equations on an unstructured moving mesh, as described in detail in Springel (2010). The mesh is defined as the Voronoi tessellation of a finite set of points that are distributed in the simulation volume. A finite volume approach for hydrodynamics is formulated on this mesh, based on a Godunov-type scheme with second-order accurate reconstruction and an exact Riemann solver applied to all interfaces for estimating hydrodynamical fluxes.

If the mesh-generating points are kept stationary, this hydrodynamical solver is equivalent to the MUSCL-Hancock second-order accurate scheme widely employed in many Eulerian hydrodynamics codes on Cartesian meshes. In fact, this equivalence can be made exact if the mesh-generating points are arranged on a Cartesian grid, in which case the cells of AREPO also become Cartesian. We will carry out some of our simulations in this mode, which we shall refer to as “fixed-mesh”. However, the novel aspect of AREPO is that the mesh-generating points are allowed to move freely, without producing problematic mesh-twisting effects. In particular, the points can be moved with the local fluid velocity itself, thereby producing an adaptive, quasi-Lagrangian behaviour. In this “moving-mesh” mode, advection errors are greatly reduced and become in fact independent of the presence of a possible bulk flow, making the results of AREPO manifestly Galilean-invariant, unlike ordinary Eulerian codes.

AREPO can additionally employ on-the-fly refinement and derefinement operations of its mesh, similar to adaptive mesh refinement (AMR) methods. We invoke this in our moving-mesh simulations to guarantee that the mass resolution is always approximately constant, as in the SPH simulations that we compare with. To this end, cells are (de)refined if their mass deviates by more than a factor of two from the desired target mass resolution (which is the initial cell mass). We note however that such (de)refinement operations are only rarely needed because the Lagrangian mesh motion already yields a nearly constant mass per cell. We also make use of AREPO’s mesh regularization feature, where mesh-generating points of highly distorted cells may receive an additional small velocity component towards the geometric center of their cell. This results in a more regular mesh, which reduces errors in the linear reconstruction step.

We note that the AREPO code has recently been successfully used in first science applications, studying first star formation (Greif et al. 2011) and galaxy formation (Vogelsberger et al. 2011). There also already exist extensions to include magnetohydrodynamics (Pakmor et al. 2011), radiative transfer (Petkova & Springel 2011), as well as treatment of the full Navier-Stokes equations (Muñoz et al. 2012).

2.1.2 Smoothed particle hydrodynamics

Smoothed particle hydrodynamics (SPH) is a particle-based approach to fluid dynamics which is popular in astronomy due to its geometric flexibility, automatic adaptivity, and good conservation properties (see e.g. Rosswog 2009; Springel 2010, for recent reviews). We use the simulation code GADGET-3 (last described in Springel 2005) for our SPH simulations, which employs a “standard” formulation of SPH with fully adaptive smoothing lengths and a simultaneous conservation of entropy and energy (Springel

& Hernquist 2002). We note however that there are many alternative formulations of SPH, some of them quite recently proposed to address certain accuracy problems of SPH (Price 2008; Read et al. 2010; Read & Hayfield 2011; Heß & Springel 2010). Our results may not necessarily apply to all of these flavours.

In some of our simulations, we also study the influence of numerical parameters in SPH on our results, such as the number N_{sph} of smoothing neighbours and the artificial viscosity parameterization. In GADGET-3, the SPH smoothing lengths h_i of particles are adjusted such that $(4\pi/3)h_i^3\rho_i = N_{\text{sph}}\bar{m}$ is always fulfilled, where h_i is the radius at which the smoothing kernel drops to zero, ρ_i is the density estimate of the particle i , and \bar{m} is the target mass resolution (here equal to the SPH particle masses). In our default 3D simulations we use $N_{\text{sph}} = 64$ smoothing neighbours.

The artificial viscosity is implemented as a viscous force:

$$\left. \frac{d\mathbf{v}_i}{dt} \right|_{\text{visc}} = - \sum_j m_j \Pi_{ij} \nabla_i \bar{W}_{ij}, \quad (1)$$

where \bar{W}_{ij} is the arithmetic average of the smoothing kernels and Π_{ij} parameterizes the viscous tensor. We use the following form (Monaghan 1997; Springel 2005) for Π_{ij} in our default runs:

$$\Pi_{ij} = - \frac{\alpha (c_i + c_j - 3w_{ij}) \cdot w_{ij}}{2 \rho_{ij}}, \quad (2)$$

with $w_{ij} = \mathbf{v}_{ij} \cdot \mathbf{r}_{ij} / |\mathbf{r}_{ij}|$ if $\mathbf{v}_{ij} \cdot \mathbf{r}_{ij} < 0$, otherwise $w_{ij} = 0$. For this definition of w_{ij} , the artificial viscosity is always repulsive, and is non-zero only if a pair of particles approaches each other, implying that the entropy produced by the viscosity is positive definite.

One general problem of artificial viscosity parameterizations is that they may introduce spurious viscosity also outside of shocks, in regions where it should in principle not be needed (e.g. Cullen & Dehnen 2010). This can be a significant problem in shear flows, where this effect may lead to unwanted angular momentum transport. To suppress the artificial viscosity in regions of strong shear, Balsara (1995) proposed a simple viscosity limiter in the form of an additional multiplicative factor $(f_i + f_j)/2$ for the viscous tensor, defined as

$$f_i = \frac{|\nabla \cdot \mathbf{v}|_i}{|\nabla \cdot \mathbf{v}|_i + |\nabla \times \mathbf{v}|_i}. \quad (3)$$

This limiter is often used in cosmological SPH simulations and also available in the GADGET code. In our default simulations with fixed α , we have refrained from enabling it, but we have also run comparison simulations where it is used, as discussed in our results section.

In addition, we consider a so-called time variable artificial viscosity, as first proposed by Morris (1997). The idea is here to try to reduce the viscosity in regions away from shocks such that it is applied in a more targeted fashion only where it is really needed. We employ the implementation of Dolag et al. (2005) in the GADGET code, where α is replaced with an individual parameter $\alpha_i(t)$ for each particle:

$$\frac{d\alpha_i}{dt} = - \frac{\alpha_i - \alpha_{\text{min}}}{\tau} + S_i. \quad (4)$$

The time evolution is controlled by a source term S_i that ramps up the viscosity quickly when a fast compression is detected, and a decay function that makes the viscosity decline again in smooth regions of the flow to a small minimum value α_{min} over the decay time τ . We note that a near-identical formulation has also been used by Price (2012).

2.2 Turbulent driving

In this work, we consider isothermal gas in which turbulence is induced through an external stochastic forcing on large scales. The condition of isothermality is not crucial for our study of subsonic turbulence, but it conveniently prevents that the turbulent kinetic energy dissipated in the flow leads to a gradual increase of the pressure in the gas with time. Instead, the dissipated energy is simply lost from the isothermal system, so that a statistically quasi-stationary state of developed turbulence can be reached after some time, where on average the energy injected on large scales is lost on smaller scales by dissipation.

Our method for calculating the acceleration field follows closely the procedure used in Schmidt et al. (2006); Federrath et al. (2008, 2009); Federrath et al. (2010) and Price & Federrath (2010). In particular, the acceleration field is setup in Fourier space and only contains power in a small range of low frequency modes between $k_{\min} = 6.27$ and $k_{\max} = 12.57$. The relative amplitude of the forcing modes over this small range is varied as $P(k) \propto k^{-5/3}$. Except in our run at $\mathcal{M} \sim 8.4$, $P(k)$ is a paraboloid centred around $(k_{\min} + k_{\max})/2$ with $k_{\min} = 6.27$ and $k_{\max} = 18.85$. The phases of the Fourier modes are drawn from an Ornstein–Uhlenbeck process and are periodically updated after a time interval Δt . The corresponding random sequence is given by

$$\mathbf{x}_t = f \mathbf{x}_{t-\Delta t} + \sigma \sqrt{(1-f^2)} \mathbf{z}_n, \quad (5)$$

where f is a decay factor given by $f = \exp(-\Delta t/t_s)$, with t_s being the correlation length. \mathbf{z}_n is a Gaussian random variable and σ is the variance of the Ornstein–Uhlenbeck process. The resulting sequences have zero mean, $\langle \mathbf{x}_t \rangle = 0$, and their correlations are given by $\langle \mathbf{x}_t \mathbf{x}_{t+\Delta t} \rangle = \sigma^2 f$. The frequent but correlated changes of the acceleration field as a function of time result in a smoothly varying turbulent driving field.

We use a purely solenoidal driving in this study, which can be obtained by projecting out the compressive part of the acceleration field through a Helmholtz decomposition in k -space. The projection operator is given by

$$\hat{\mathbf{a}}(\mathbf{k})_i = \left(\delta_{ij} - \frac{k_i k_j}{|k|^2} \right) \hat{\mathbf{a}}_0(\mathbf{k})_j \quad (6)$$

in Fourier space. We note that solenoidal driving appears particularly appropriate for subsonic turbulence. Compressive modes would only cause additional sound waves and only start to couple to smaller modes once non-linear steepening of these acoustic waves becomes important. In any case, if a compressive component was added, we would expect a somewhat broader density PDF for a given Mach number (Federrath et al. 2008).

Finally, the acceleration field due to the driving mechanism is calculated in position space at each particle or cell position directly as a sum over the small number of non-zero Fourier modes, a procedure which is free of any resolution limitations. This field is then introduced as an additional source term in the Euler equations, in the same way as an external gravitational field is normally coupled to gas dynamics. In our time-integration scheme, the external acceleration is added in two half-steps at the beginning and end of each timestep, producing a leap-frog type integration scheme.

2.3 Simulation set

We consider periodic boxes of unit length on a side, filled with isothermal gas at unit mean density and unit sound speed ($\bar{\rho} = c_s = 1$). The Euler equations are scale-independent, so that once

quasi-stationary turbulence has developed the only characteristic parameter remaining is the mean Mach number \mathcal{M} , which we define as the mass-weighted rms-velocity relative to the sound speed. The amplitude of the driving field determines \mathcal{M} , and can in principle be freely adjusted to reach the desired strength of turbulence. We note that we have here not attempted to subtract the mean gas velocity in our simulations even though a respectable amount of bulk motion can be generated in the supersonic regime as a result of our driving. In fact, the kinetic energy of the bulk motion can become at times nearly as large as the kinetic energy of the irreducible smaller scale motions, and hence matters when measuring the mean Mach number in terms of the total kinetic energy. The bulk motion is negligible in the subsonic regime. As the bulk motion however only affects the DC mode in Fourier space, it has no influence on our power spectrum measurements. The Mach numbers we report are corrected for the bulk motion and do not include it.

For technical reasons having to do with our measurement technique for dissipation discussed below, we actually do not use an exact isothermal equation of state, but rather one with an adiabatic index of $\gamma = 1.001$, combined with enforcing the entropy of the gas to stay at the initial value after completion of each timestep. Specifically, for a prescribed initial mean density $\bar{\rho}$, and an (isothermal) sound speed c_s , we initialize the gas with a specific entropy

$$\bar{A} = c_s^2 \bar{\rho}^{1-\gamma}, \quad (7)$$

hence the pressure is given by

$$P_i = \bar{\rho} c_s^2 \left(\frac{\rho_i}{\bar{\rho}} \right)^\gamma \quad (8)$$

for a cell/particle of density ρ_i . The specific internal energy per unit mass, u_i , can be calculated from the specific entropy as

$$u_i = \bar{A} \frac{\rho_i^{\gamma-1}}{(\gamma-1)}. \quad (9)$$

In our ‘quasi-isothermal’ simulations, the entropy of the gas is reset to \bar{A} after each timestep, so that the pressure of a particle/cell is always given by equation (8). All our simulations are started from a regular Cartesian grid of particles with initially zero velocities, and use a global time step for all particles/cells.

Each of our primary subsonic simulations was performed with three different numerical methods: SPH as implemented in the GADGET-3 code, moving-mesh hydrodynamics using AREPO, or fixed-mesh Eulerian hydrodynamics also based on AREPO but with a stationary Cartesian mesh. The resolution of our simulations ranges from 64^3 to 512^3 particles or cells, respectively. Table 1 gives an overview of these simulations, and lists their most important parameters. Our naming convention is such that a leading capital letter indicates the type of a simulation (‘S’ for SPH, ‘A’ for moving-mesh with AREPO, and ‘F’ for a fixed mesh), followed by a digit that indicates the resolution level (‘1’ for 64^3 , ‘2’ for 128^3 , etc.). When we compare different simulation techniques or different numerical resolutions, we always do this at identical driving amplitude, such that any difference that is seen arises from the hydrodynamics alone. In particular, all of our subsonic simulations (where $\mathcal{M} \sim 0.3$) use an identical turbulent forcing field.

In our default SPH simulations, we consider two different artificial viscosity formulations, one with a viscosity strength parameter equal to $\alpha = 1$, the other with a time-variable viscosity that is individual for each particle (both with and without a shear viscosity limiter). These choices approximately bracket the range of viscosity settings that are in use in production calculations in cosmology. In order to examine the dependence of our results on numerical parameters of SPH in more detail, we have additionally

performed a set of SPH simulations with further variations in the artificial viscosity parameters ($\alpha = 1.0$ with a shear viscosity limiter, $\alpha = 0.1$, $\alpha = 0.01$, $\alpha = 0.001$, and $\alpha = 0.0001$). Furthermore, we have also studied the influence of the number of SPH smoothing neighbours. Our default value for N_{ngb} is 64, but we also used $N_{\text{ngb}} = 180$ and $N_{\text{ngb}} = 512$. The corresponding simulation runs and their symbolic names are summarized in Table 2.

2.4 Measuring dissipation

The classical theory of Kolmogorov for incompressible turbulence conjectures that energy is injected on large scales and then cascades down to eddies of ever small size, until dissipation on very small scales eventually occurs. In this picture, large scale gas motions in the resulting turbulent cascade do not dissipate energy in any significant way, instead the energy is essentially transported in a conservative fashion over the inertial range down to the dissipation scale. In the analysis of numerical turbulence simulations it is standard procedure to examine how the kinetic energy is distributed as a function of scale, which is usually done in terms of the velocity power spectrum. We suggest here that it is also interesting to try to directly measure the energy dissipation as a function of scale, as this provides interesting complementary information about the dissipative properties of a numerical scheme.

To this end, we define dissipation as the irreversible conversion of kinetic energy into heat. Because we use $\gamma = 1.001$ in our ideal gas equation-of-state, dissipation manifests itself as an increase in the specific entropy of a cell or a particle. To measure this quantity, we compare A_i after completion of every timestep with the value \bar{A} , afterwards resetting A_i to \bar{A} . The extracted thermal energy, $\Delta E_i = m_i(A_i - \bar{A})\rho_i^{\gamma-1}/(\gamma - 1)$, is then the *dissipated* energy, which we assume to leave the system in concordance with the quasi-isothermal conditions we impose.

In SPH, A_i only changes due to the artificial viscosity and is easily obtained from the work done against the artificial viscosity forces. The ΔE_i measured for a SPH particle is always positive definite in this case. In our mesh-code AREPO, exact energy-, mass- and momentum-conservation is given in every hydrodynamic step. To measure the dissipative increase of entropy of a cell, we additionally advect the entropy in the system in a conservation fashion, as described by Springel (2010). The dissipative energy change ΔE_i of a cell can then be estimated in the above fashion, with the caveat that the energy ΔE_i is not guaranteed to be positive definite for all cells due to discretization errors. However, in this case a local average over a group of cells will still give a faithful estimate of the total energy that is lost, due to the manifestly conservative properties of the mesh-based evolution of the fluid. We shall use the ΔE_i values for a Fourier analysis of the spatial scales on which most dissipation occurs, and for cross-checking whether the total dissipated energy balances the total injected energy when steady-state turbulence is reached.

2.5 Power spectrum measurements

The 3D power spectrum of a scalar or vector field w is defined as the Fourier transform of the two-point correlation function

$$C_w(\mathbf{l}) = \langle w(\mathbf{x} + \mathbf{l})w(\mathbf{x}) \rangle_{\mathbf{x}}. \quad (10)$$

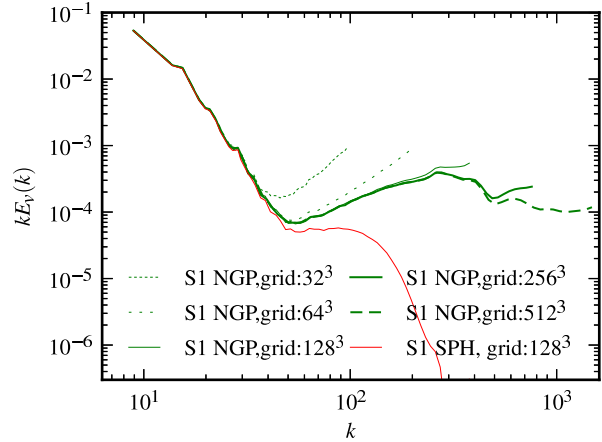


Figure 1. Results for different approaches to measure the velocity power spectrum for one of our 64^3 SPH simulations. The green lines with different line styles show our nearest point sampling, with sampling resolutions 32^3 , 64^3 , 128^3 , 256^3 and 512^3 . The results for 128^3 (our default grid size at this resolution) and higher are virtually identical up to the Nyquist frequency of the run. The red line shows a measurement when the velocity field is calculated by SPH-smoothing for a 128^3 mesh. This method (advocated by Price 2012) suppresses small-scale velocity noise but also removes kinetic energy associated with particle motions on these scales.

Thus

$$E_w(\mathbf{k}) = \frac{1}{(2\pi)^3} \int_V C_w(\mathbf{l}) \exp(-i\mathbf{k}\mathbf{l}) d^3\mathbf{l} \quad (11)$$

$$= \left(\frac{2\pi}{L}\right)^3 |\hat{w}(\mathbf{k})|^2, \quad (12)$$

where \hat{w} is the Fourier transform of w . In order to numerically estimate \hat{w} , the field w is usually represented in discretized form on a Cartesian grid, allowing an efficient measurement of the power spectrum through discrete Fourier transforms.

We here use a nearest neighbour sampling of the intrinsic hydrodynamical quantities of the particle/cell data of our simulations to do this. The value of the desired quantity w at each grid cell is hence obtained as the value of the particle or cell closest to the centre of a grid cell. This simple approach aims to maximize the information content extracted from the simulations, but risks to suffer from power aliasing effects if the employed Fourier grid is too small. We have however checked that our default Fourier mesh size we employ for our power spectrum measurements (based on a grid twice as fine as the resolution of the simulation at hand) is fine enough to make such effects negligible.

Another important aspect of our power spectrum measurement is that it faithfully represents the total kinetic energy of the particle/cell set. This should be given as the integral over the measured power spectrum. According to Parseval's theorem, this integral is equal to the variance of the velocity field that is used to measure the spectrum through a discrete Fourier transform. As our velocity field definition creates a fair sample of the particle/cell velocity values, we obtain an accurate accounting of the total kinetic energy in the flow. In contrast, smoothing the SPH velocity field via kernel interpolation as advocated by Price (2012) removes kinetic energy on small scales and can cause a significant error in the total energy represented by the power spectrum measurement. This is explicitly demonstrated in Figure 1, where we show a power spectrum measurement for one of our 64^3 SPH simulations carried out

with different techniques. The green lines with different line styles show our nearest point sampling, with resolutions 32^3 , 64^3 , 128^3 , 256^4 and 512^3 . The results for 128^3 and higher are virtually identical up to the Nyquist frequency of the run and accurately reflect the total kinetic energy of the particle set. On the other hand, if we SPH-smooth the velocity field on a 128^3 mesh, we obtain the red solid line. While this method suppresses small-scale velocity noise, it also reduces the kinetic energy in the field by $\sim 3.6\%$ in this case. However, if for example our S1-tav simulation is considered the suppressed energy amounts to about $\sim 13\%$ of the total kinetic energy due to the higher power on smaller scales in that simulation. We note that we calculate our power spectrum measurements on-the-fly while the turbulence simulations are run, allowing us to reach a very fine temporal resolution for the evolution of the power spectrum of the different quantities we examine.

Assuming an isotropic statistical distribution, the 1D power spectrum of the quantity w can then be obtained by angular averaging $E_w(\mathbf{k})$ over shells in k -space, as

$$E_w(k) = 4\pi k^2 \langle E_w(\mathbf{k}) \rangle \quad (13)$$

where $k = |\mathbf{k}|$. We employ fine logarithmic bins in k for determining the mean power per mode at a certain k , with bins combined as needed such that a minimum number of modes per k -bin is obtained. The normalization of the 1D power spectrum is chosen such that the integral over the power spectrum gives always the total power, i.e.

$$\sigma^2 = \int E_w(k) dk = \frac{1}{N^3} \sum_{j,k,l=0}^{N-1} |w_{ijk}|^2. \quad (14)$$

We note that we usually plot the quantity $kE_w(k)$ in our power spectrum plots as a function of $\log k$, instead of using $E_w(k)$ directly. This has the advantage that a horizontal line in such a plot corresponds to constant total power per logarithmic decade, one with a positive slope means that small scales dominate, whereas a negative slope indicates that the total power in the examined quantity is dominated by large scales.

Finally, we want to clarify how we measure the power spectrum of the energy dissipation rate, which requires a special treatment. In order to allow for a direct comparison with the kinetic energy power spectrum obtained from $w = \mathbf{v}$, we in principle want to set $w = \sqrt{\Delta E}$, where ΔE is the energy dissipation rate measured as described above. However, since the measured dissipation rate can sometimes exhibit negative values in the case of the mesh code, this procedure needs to be modified. We thus compute the power spectrum for $w_+ = \sqrt{\Delta E_+}$ and $w_- = \sqrt{\Delta E_-}$ separately, where $\Delta E_+ = \min(\Delta E, 0)$ and $\Delta E_- = \max(\Delta E, 0)$ are the positive and negative parts of the measured dissipation field. Finally, the dissipation power spectrum is then estimated as

$$E_{\text{diss}}(k) = E_{w_+}(k) - E_{w_-}(k). \quad (15)$$

Note that the k -integral of this quantity is equal to the total energy dissipation rate.

3 SUBSONIC TURBULENCE

3.1 Global characteristics

In Figure 2, we show the time evolution of the rms Mach number for our runs of subsonic turbulence at a resolution of 256^3 (S3, S3-tav, A3, and F3). After an initial ramp up of the turbulent energy, a quasi-stationary state is established, starting at time $t \sim 5 - 10$.

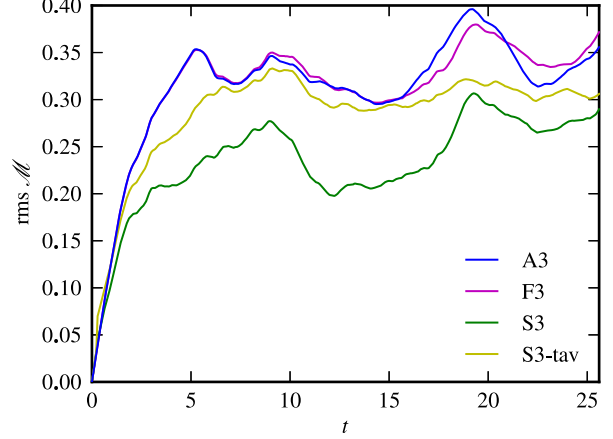


Figure 2. Mean Mach-number evolution as a function of time for our subsonic turbulence simulations. Here \mathcal{M} is defined as the mass-weighted rms velocity in units of the sound speed. The different lines give results for SPH (green and yellow), AREPO (blue), and a fixed-mesh (magenta), at a resolution of 256^3 particles/cells (runs at different resolutions give extremely similar results). We see that a quasi-stationary state is reached after time $t \sim 10$, but the total kinetic energy in the $\alpha = 1.0$ SPH case (green) is somewhat smaller than in the two mesh codes and in the SPH run with time-variable artificial (tav) viscosity (yellow).

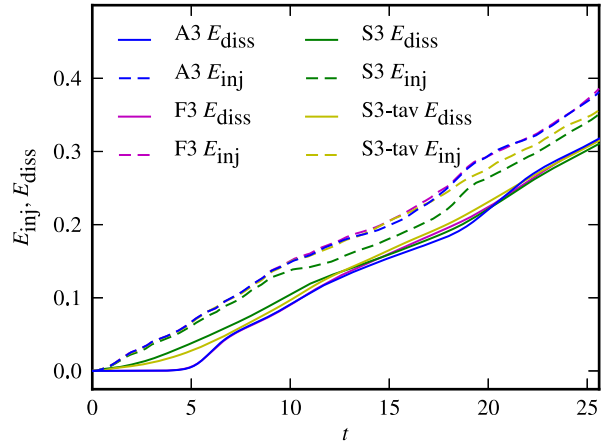


Figure 3. Time evolution of the total cumulative injected energy (dashed lines) and the total dissipated energy (solid lines), for different simulation runs, as labeled. At any given point in time, the difference between the injected energy and the dissipated energy is the kinetic energy stored in the simulation box. The time average energy dissipation rate per unit mass is $\epsilon \simeq 0.016$.

There are however still substantial intermittent fluctuations in the global rms Mach number, making it clear that averaging over extended periods of time is required to obtain truly stable results for the statistical properties of the turbulent fluid state, especially on large scales. We note that runs carried out with different numerical resolutions give extremely similar results to the ones shown in Fig. 2. Interestingly, the time evolutions of the moving-mesh and the fixed-mesh results agree very well with each other, but the terminal Mach number reached by SPH is significantly lower, especially in the run with $\alpha = 1.0$. This is despite the fact that the driving field imposes exactly the same accelerations in all the sim-

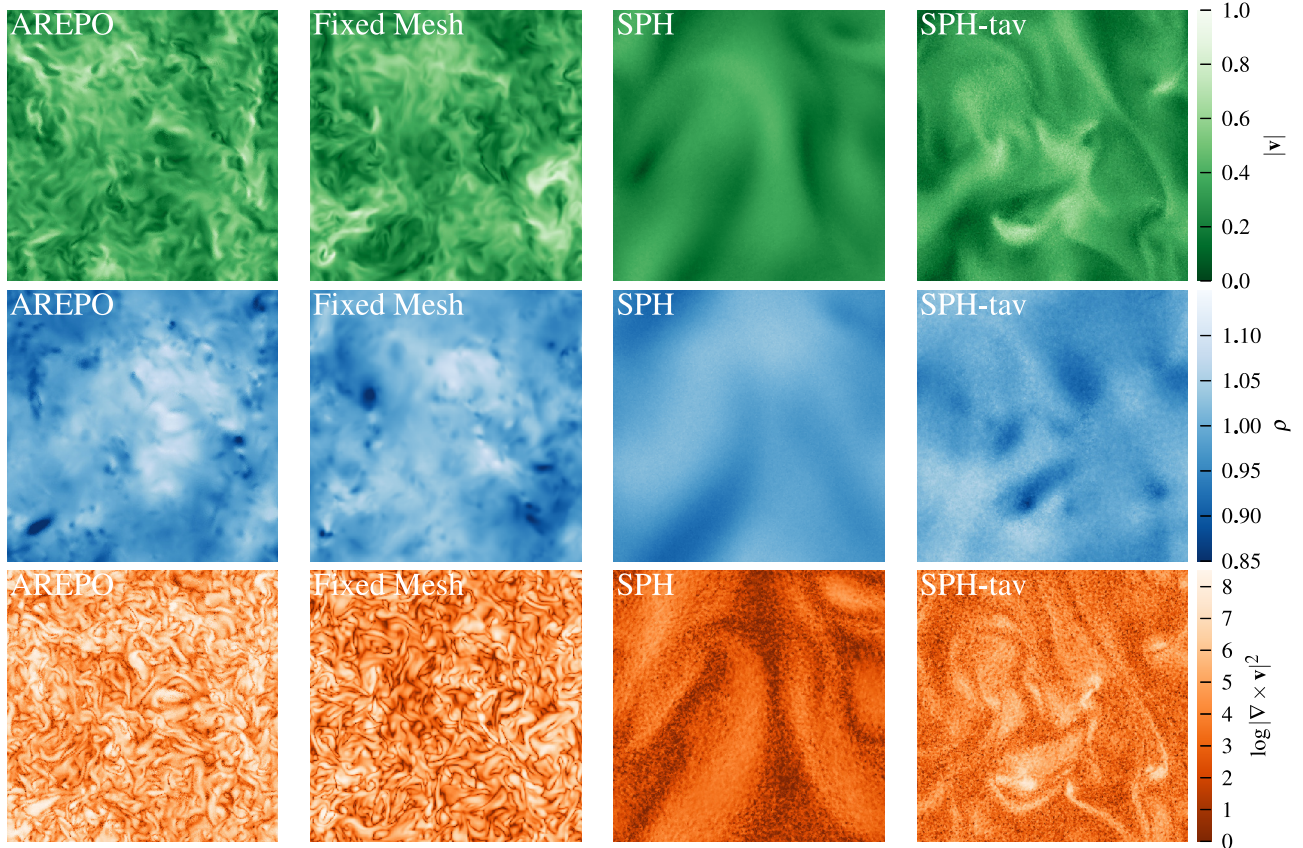


Figure 4. Visual comparison of the turbulent velocity field (top row), the density field (middle row) and the enstrophy $|\nabla \times \mathbf{v}|^2$ (bottom row) in quasi-stationary turbulence with $\mathcal{M} \sim 0.3$, simulated with different numerical techniques. Shown are thin slices through the middle of the periodic simulation box at the final time $t = 25.6$. From left to right, we show our moving grid result (A3), an equivalent calculation on a static mesh (F3), and two SPH calculations, one with a fixed $\alpha = 1.0$ viscosity (S3) and the other with time-variable viscosity (S3-tav), as labeled.

ulations. The smaller overall kinetic energy achieved in the SPH run with $\alpha = 1.0$ is a result of viscous damping of large-scale modes at or close to the driving scale. This effect is greatly reduced but not completely eliminated with the time-variable viscosity parameterization.

We show the cumulative injected and dissipated energy as a function of time in Figure 3 for the same simulations. Note that the difference between these two quantities is exactly the kinetic energy stored in the gas at the corresponding time. Interestingly, the mesh-based simulations do hardly dissipate any energy until $t = 5$, in contrast to the SPH simulations which show signs of energy dissipation right from the start. This is consistent with the impression from Figure 2 that it is harder in SPH than in the mesh-code to set the largest eddies into motion. At around $t \sim 13$, the total cumulative dissipated energies begin to be rather similar for all three methods, but the total injected energy of the SPH simulations still lags behind the mesh-based runs. This is simply because the lower velocities in SPH reduce the average value of $\langle \mathbf{v} \mathbf{a}_{\text{driv}} \rangle$, where \mathbf{a}_{driv} is the acceleration due to the external driving field. As a result,

the kinetic energy in the SPH runs never fully manage to close the gap to the mesh-based calculations.

3.2 Visualizations of the turbulent velocity, kinetic energy density and vorticity fields

To better understand the systematic differences between the simulation techniques, it is instructive to consider maps of fluid quantities in slices through the simulation cube. To construct them, we use nearest neighbour sampling at the coordinates of a two-dimensional grid with 512^2 pixels, twice finer than the nominal resolution of the simulations examined here. Each pixel will hence show the value of the closest mesh cell or SPH particle, respectively. This directly reflects the individual fluid elements used in the discretization schemes of the two numerical techniques, highlighting mesh or sampling artefacts if they exist, as well as discretization noise.

In the top row of Figure 4, we show slices of the velocity field at the final time $t = 25.6$ of our subsonic turbulence simulations, comparing the moving-mesh calculation with AREPO to the one with a fixed Cartesian mesh, and to our SPH simulations with

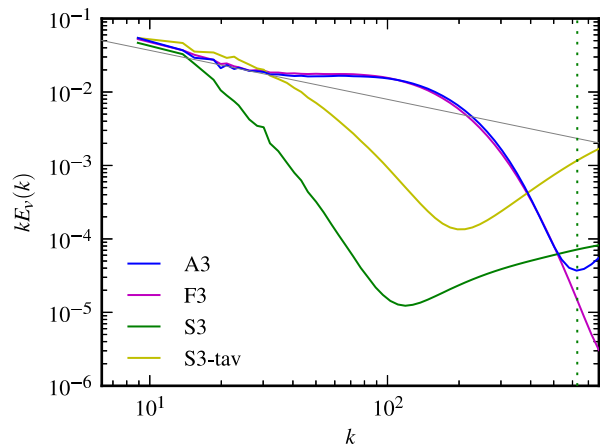


Figure 5. Velocity power spectrum of SPH and AREPO, compared at a resolution of 256^3 . The thin grey line shows the slope expected for Kolmogorov’s theory of incompressible turbulence. The power in SPH falls much more rapidly than expected for fully developed turbulence. On small scales, the power rises again quite strongly up to the Nyquist frequency. This is small-scale velocity noise characteristic of SPH. The vertical green dotted line indicates the scale $2\pi/h_{\max}$, where h_{\max} is the maximum SPH smoothing length among all the particles.

$\alpha = 1.0$ and time-variable viscosity. We can see that the slices of the moving mesh (top left panel) and the fixed mesh calculations (top middle panel) appear qualitatively very similar, featuring both large-scale coherent motions and many irregular small-scale features. The moving-mesh result appears slightly less smooth and shows more small-scale features, but based on these images alone it would be hard to decide whether this is due to a higher effective resolution or due to the more irregular shaped cells in the Voronoi case, which may induce some aliasing effects in the pixelized map.

In contrast, the nearest neighbour SPH results for the velocity field, shown in the two panels on the top right, look dramatically different. Here the corresponding velocity fields do not contain the small-scale velocity features present in the mesh-based calculations, particularly in the $\alpha = 1.0$ run, suggesting that an equally well developed turbulent cascade has not really formed in the SPH simulation.

This impression is compounded by slices through the density and enstrophy fields ($|\nabla \times v|^2$), shown in the middle and bottom row of Figure 4, respectively. While the mesh-based calculations exhibit a delicate mix of fine structures in the kinetic energy density both on large and small scales, the SPH $\alpha = 1.0$ simulation shows only some large-scale motions, presumably reflecting primarily the driving field. While the S3-tav run shows more structures, there is still a paucity of smaller flow features. Similarly, whereas the enstrophy slices reveal a granular structure in the vorticity field that is dominated by small structures, these are essentially completely absent in the SPH calculations. The utilization of a time dependent artificial viscosity scheme improves the SPH result noticeably. A further improvement might be achieved through more advanced viscosity switches, like those suggested by Cullen & Dehnen (2010) or Read & Hayfield (2011).

3.3 Velocity power spectra of subsonic turbulence

A more quantitative analysis of this difference is obtained by considering velocity power spectra of these four different simulation

techniques. In Figure 5, we compare power spectra of the kinetic energy for our runs at 256^3 resolution, averaged over an extended period of time from $t = 10$ to $t = 25.6$, after a quasi-stationary turbulent state has been established.

The results confirm the impression inferred from the previous subsection. There is a rather striking difference between the mesh-based simulations and our SPH calculations. The kinetic energy in SPH is already drained at rather large scales, such that an extended energy cascade is not formed. The self-similar turbulent power spectrum expected based on Kolmogorov’s theory for incompressible turbulence ($E_v(k) \propto k^{-5/3}$) is indicated as a thin grey power law in the figure – this line has a different slope compared with the rapid decline of the power spectrum observed in SPH.

In contrast, the mesh-based simulations show a slope similar to the expected Kolmogorov law, at least on very large scales. Fits to the power-law region of the velocity power spectrum give slopes of -1.64 and -1.68 for the moving mesh and the fixed mesh, respectively, whereas SPH shows a wrong slope of -4.14 in the case of a constant artificial viscosity and -2.1 in the case of a time-dependent artificial viscosity. There is even an excess of power in the mesh-based results above the expected continuation of the Kolmogorov slope, before the velocity power spectrum eventually starts to rapidly decline on scales somewhat larger than the Nyquist frequency corresponding to the nominal spatial resolution. This bump in power is a manifestation of the so-called bottleneck effect, which is commonly encountered close to the resolution limit in mesh-based studies of turbulence and is also seen in experiments (e.g. Meyers & Meneveau 2008, and references therein). The numerical bottleneck effect is similar to the physical bottleneck effect and considerably complicates attempts to robustly measure the true slope of the inertial range of turbulence, as this requires the use of extremely high resolution (2048^3 and beyond), such that the bottleneck bump moves to sufficiently small scales. We note that the moving-mesh and fixed-mesh calculations agree well with each other up to quite high k , where eventually some small differences arise, caused by the different mesh geometries and truncation errors in the two schemes.

Another interesting feature of the SPH velocity power spectrum is that there is actually a minimum at some intermediate scale, followed by a strong rises towards still smaller scales. The minimum occurs on scales that should formally still be well resolved, because these scales are considerably larger than the maximum SPH smoothing length h_{\max} among all the particles (indicated as the vertical green dotted line at $2\pi/h_{\max}$ in Fig. 5). Nevertheless, already on this comparatively large scale, the power starts to increase again. This is a result of the high small-scale subsonic velocity noise present in SPH that we already witnessed in Figure 4. Even when a kernel-smoothed velocity field is considered instead, and the power spectrum is calculated for this smoothed quantity, there is a considerable small-scale bump left, as shown by the dashed green line which shows the power spectrum of the SPH-smoothed velocity field. On large scales, the behaviour of this field is the same as for the nearest neighbour interpolated one, as expected.

In Figure 6, we show a resolution study for the subsonic velocity power spectra of our AREPO and SPH runs, ranging from 64^3 to 512^3 particles/cells. The SPH simulations seem to converge to each other only on the largest scales. Even with a resolution as high as 512^3 particles, there is build up of an extended inertial range with the expected energy cascade. We only see that with improving resolution there is a slight shift towards smaller scales of the rapid

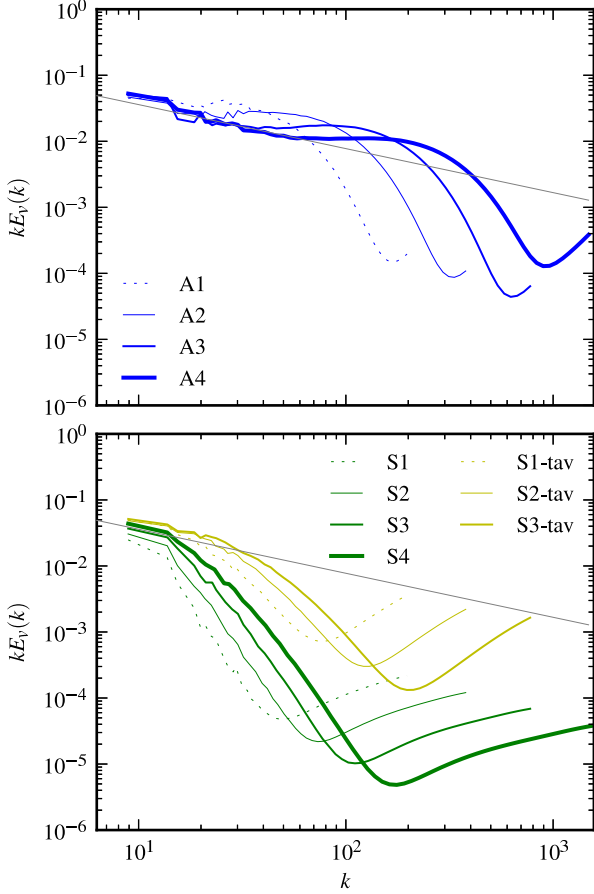


Figure 6. Convergence study for the velocity power spectrum of $\mathcal{M} \sim 0.3$ subsonic turbulence. The panel on top shows results for AREPO, from a resolution of 64^3 to 512^3 cells. The panel on the bottom gives the corresponding results for SPH. However, even at a high resolution as high 512^3 particles, no extended inertial range of turbulence can be identified in SPH. The thin grey lines show the power-law expected for Kolmogorov’s theory.

decline of the power spectrum. Also, the minimum of the power spectrum is reached at progressively smaller scales, but the overall shape of the velocity power spectrum does not improve significantly, and the small-scale noise bump remains present.

For the simulations with AREPO, we observe that the bottleneck effect moves to smaller scales with improving resolution. This is expected, as this effect should be tied to the numerical dissipation occurring on scales close to the resolution limit. As the bottleneck moves towards smaller scales, a larger inertial range with a self-similar power-law region is established on large scales. We note that the rise of the power in the moving mesh-code on very small scales, at around the Nyquist frequency, is due to noise and aliasing effects at the spatial resolution limit that is reached here, which is qualitatively a very different effect from the small-scale velocity noise that sets in in SPH on much larger scales.

The computational cost of one of our moving-mesh turbulence simulations with AREPO in the sub-sonic regime is nearly a factor of 4 higher than a corresponding SPH simulation with GADGET-3 at the same number of resolution elements. Compared to a corresponding fixed-mesh calculation, the moving-mesh simulation is about 5 times slower. This difference arises mainly due to the costly Voronoi mesh construction, and in the case of moving ver-

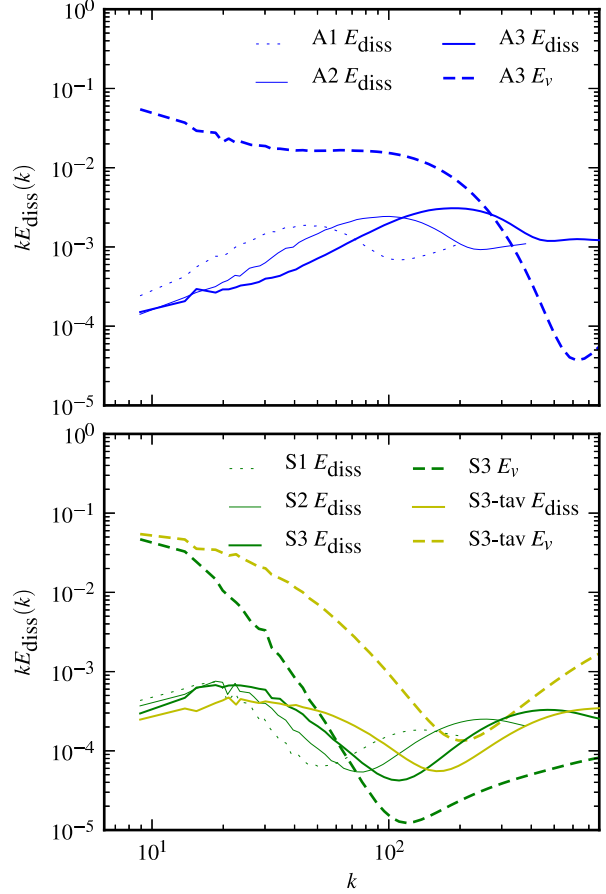


Figure 7. Dissipation power spectra for AREPO and SPH runs at different resolutions, compared to the corresponding shape of the velocity power spectrum at 256^3 resolution (dashed lines). For the mesh-code, the dissipation actually peaks on scales where the power spectrum starts to deviate from Kolmogorov’s self-similar scaling. In contrast, SPH shows very strong dissipation already on larger scales, preventing the build-up of a turbulent cascade. In addition, the dissipation is also strong on small scales, close to the resolution limit, where the small-scale noise developing in SPH is constantly damped away.

sus fixed mesh, additionally due to the roughly twice as many Riemann problems that need to be solved for the unstructured Voronoi mesh compared with a Cartesian grid. However, these differences in run time of order unity are implementation dependent and ultimately of limited importance. What should really be considered is the computational cost to reach a desired level of accuracy. For example, as our moving mesh run with 128^3 cells (A2) produces a model for the Kolmogorov spectrum at least as good as the SPH run with 256^3 particles (S3), one may state that AREPO is actually about 4 times as efficient as SPH when comparing these two runs. But we caution that such statements about the relative efficiency of different schemes are in general resolution and problem dependent. For example, as we shall argue below (subsection 3.6), we expect that the efficiency gain of AREPO relative to SPH at fixed accuracy actually grows with Reynolds number. Also, the relative cost of moving-mesh vs. fixed-mesh depends on the Mach number of the turbulence, because for highly supersonic flows considerably smaller timesteps are needed for a fixed mesh compared with a moving mesh. Finally, we remark that in astrophysical applications

that include self-gravity the run time difference between AREPO and GADGET at the same number of resolution elements shrinks considerably, simply because of the comparatively high cost of the tree-based gravity calculation.

3.4 Dissipation power spectra

In Figure 7, we show power spectra for the energy dissipation rate, measured as described in Sections 2.4 and 2.5. In the top panel, we show results for the simulations A1 to A3 with resolutions 64^3 to 256^3 , averaged over the same period of time as in our velocity power spectrum plots. For comparison, we also plot the kinetic energy power spectrum as dashed lines, in order to allow a comparison of the shapes of the different curves. Interestingly, the AREPO simulations show a peak in dissipation right at the scales where the velocity power spectrum begins to rapidly fall. While there is also some residual dissipation at very large scales (which becomes smaller with better resolution), this is more than an order of magnitude lower than the energy drained around the scales where the dissipation measurement peaks. The result is hence consistent with an interpretation where only negligible dissipation occurs on large scales, with all the energy dissipated on some smaller dissipation scale, which in our case is related to the numerical resolution limit. Such a scenario is consistent with the theoretical assumptions that enter Kolmogorov’s theory of self-similar scaling.

In the bottom panel of Figure 7, we show the corresponding SPH results. Here a very different shape of the dissipation power spectrum is found. There is a peak already on very large scales, close to the driving scale. The amplitude of the dissipation lies considerably higher on these scales range than in the mesh-code, and shows only a weak dependence on numerical resolution. This explains why there is not much energy left to be fed into a turbulent cascade that could transport it conservatively towards smaller scales. Interestingly, there is however a second extended maximum of the SPH dissipation power spectrum on very small scales, coinciding with the location of the small-scale bump in the velocity power spectrum. This is apparently related to viscous dissipation of some of the small-scale velocity noise in SPH.

3.5 Dependence on SPH parameter settings

Given the sobering results we have thus far obtained for subsonic turbulence in SPH, it is an important question whether this outcome can be significantly improved with different parameter choices for the method. The primary numerical parameters that may strongly affect the SPH results are the number of smoothing neighbours, and the artificial viscosity parameterization. In fact, these are the only aspects that can be changed easily without reverting to an entirely different formulation of SPH, or a substantially different method for particle hydrodynamics.

An increase in the number of smoothing neighbours should reduce the noise in SPH kernel estimates. In fact, it has been argued that convergence of SPH requires a simultaneous increase both of the number of simulation particles and a (slower) increase of the number of smoothing neighbours (Rasio 2000; Robinson & Monaghan 2011). Unfortunately, in practice the clumping instability present for the normal SPH kernel shape counteracts attempts to improve the SPH estimates through a drastic increase of the number of smoothing neighbours (but see Read et al. 2010). Regardless, we have examined whether an increase of the number of neighbours to $N_{\text{ngb}} = 180$ or even $N_{\text{ngb}} = 512$ improves our results. To this end we have repeated our S2 simulation with these settings.

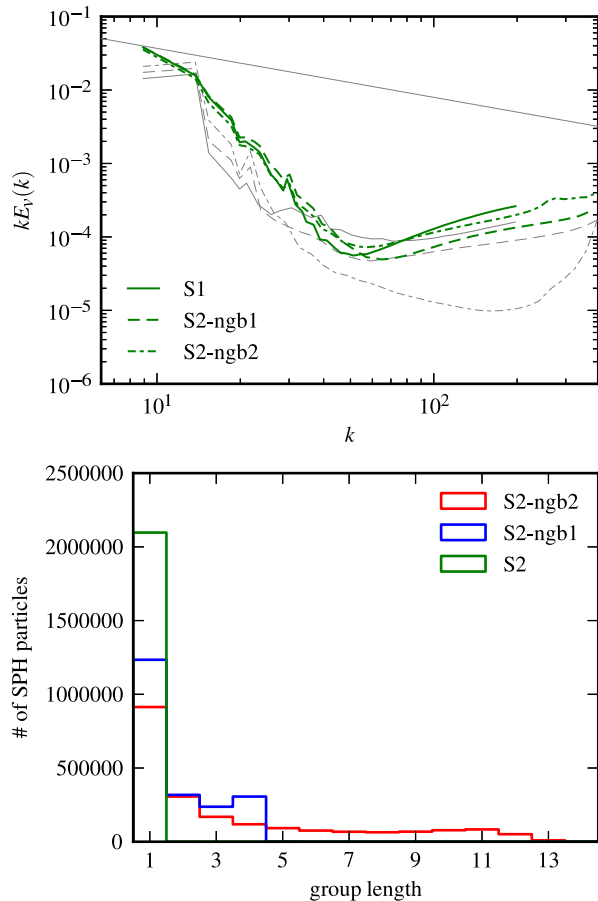


Figure 8. Effects of a larger number of SPH smoothing neighbours. The panel on top gives results for the velocity power spectrum when the number of neighbours is increased from our default of 64 to 180, and finally to 512. Formally, the later run with 128^3 particles has the same mass and spatial resolution as our S1 run with 64^3 particles. The lines shown in grey correspond to an early time, when the turbulence is not yet fully established. Here greater differences between the results can be seen, with the larger number of neighbours yielding clearly more power on large scales, and less power due to noise on small scales – this is the expected effect of a better gradient accuracy due to a larger number of smoothing neighbours. However, this advantage is quickly destroyed by the clumping instability. The bottom panel shows a histogram of SPH particle clump sizes determined with a friends-of-friends group finder, taking a linking length of 0.05 of the mean particle spacing. We see that the larger number of neighbours induces substantial clumping, reducing the number of independent sampling points and introducing large inhomogeneities in the kernel sums.

In the top panel of Figure 8, we compare the velocity power spectra of these two simulations with the S1 simulation. Note that at the resolution of 128^3 employed for these tests, the S2 run with 512 neighbours is expected to have effectively the same mass- and spatial-resolution as the S1 simulation with our default choice of 64 smoothing neighbours. Interestingly, the power spectra look very similar on large scales, i.e. there is no noticeable improvement due to the higher number of smoothing neighbours at a fixed mass/spatial resolution. Only the small-scale noise is reduced when the number of neighbours is increased. However, if we look at early times after the driving has started (grey lines in Fig. 8), larger differences are seen and the runs with a larger number of neighbours

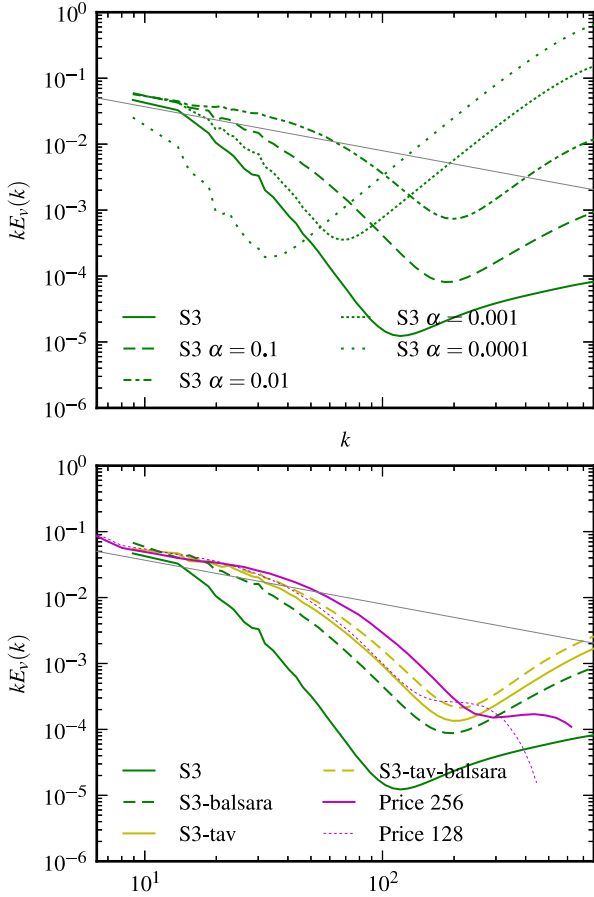


Figure 9. Dependence of SPH turbulence results on the viscosity parameterization. The top panel illustrates the effect of systematically varying the SPH viscosity strength. For lower α , the velocity power on large scales goes up, but the shape of the power spectrum does not improve. Note however that this also increases the small scale velocity noise. However, if the viscosity strength is chosen too low, the power on large scales goes down again and the power spectrum is entirely noise-dominated in this case. The bottom panel compares different artificial viscosity schemes. Enabling the Balsara viscosity suppression factor improves the power spectrum, yielding a result similar to our $\alpha = 0.1$ run. A further improvement is achieved if a time dependent viscosity parameterization is applied. For comparison, we include the results of Price (2012) for his 128^3 and 256^3 runs. The former is very close to our time-variable artificial viscosity run while the latter is comparable to our run with $\alpha = 0.01$. The thin grey lines in both panels show the slope of the expected Kolmogorov power spectrum.

do show more large-scale power, as expected for an improved accuracy.

The bottom panel of Fig. 8 highlights the reason why this advantage soon vanishes. Here we determine the size spectrum of particle clumps formed in the runs at the end of the simulated time by applying a standard FOF algorithm with a small linking length of 0.05 times the mean particle separation. Whereas in the S2 simulation with the default neighbour number essentially all particles stay isolated and no groups are found, this is very different in the runs with enlarged neighbour number. In the case of 512 smoothing neighbours, less than half of the particles remain isolated, with a large number of clumps containing multiple particles, up to ~ 10 . This is the well-known clumping instability that frustrates attempts to beat down noise in the kernel sums by simply using a large num-

ber of smoothing neighbours. Instead, the forming clumps reduce the effective resolution and the accuracy of the kernel interpolants.

We now turn to the artificial viscosity parameterization, which is another area where one may hope that simple changes could lead to significant improvements in the results obtained for turbulence. In particular, the problematic damping of the injected turbulent energy already on large scales hints that a reduction of the viscosity may help. A lower viscosity seems also warranted because in our subsonic regime shocks are not really expected, suggesting that artificial viscosity may perhaps not be needed at all, or only at a minimal level. We have hence first repeated our default simulations with a series of reduced settings of the artificial viscosity parameter, trying $\alpha = 0.1$, $\alpha = 0.01$, $\alpha = 0.001$, and $\alpha = 0.0001$. The top panel of Figure 9 shows the resulting velocity power spectra at S3 resolution. Compared to our default S3 run, the large-scale power clearly increases when the viscosity strength is reduced, but at the same time the small-scale noise also drastically increased. In fact, we find that the energy dissipated in this noise-dominated regime is essentially invariant when the viscosity is varied (see Fig. 7). While a larger artificial viscosity reduces the amplitude of the velocity noise, it also implies stronger viscous forces, such that the average work done against the viscous forces varies little.

Eventually, however, the improvement of the large-scale results when lowering the viscosity ends. Instead the results deteriorate again when the viscosity is lowered to $\alpha = 0.001$, or even $\alpha = 0.0001$. In fact, for the latter case the large-scale result is even worse than for $\alpha = 1.0$ whereas the small-scale noise is orders of magnitude larger. In this series of runs, it could be argued that $\alpha = 0.01$ is “best” in the sense that the expected Kolmogorov slope of the velocity power spectrum is approximately reproduced over the widest range of scales. The large noise on small scales and the anemic ‘dip’ in the power spectrum at $k \sim 200$, which falls short of the expected shape of the dissipation range (see below), raise significant concerns though that the statistical properties of these turbulent motions suffer from significant noise contaminations.

In the bottom panel of Fig. 9, we have instead enabled the so-called Balsara reduction factor for the viscosity in the presence of strong shear, and we consider a time-dependent viscosity parameterization. Again, both of these changes lead to an increase of the power on large scales and more noise on small scales compared to S3, as expected due to the reduced viscosity. It turns out that the Balsara switch (S3-balsara) happens to lead to an extremely similar reduction of the effective viscosity as given by our run with $\alpha = 0.1$ shown in the upper panel, but this is just by accident. Compared to these two runs, the simulations with time-variable viscosity give slightly more power on all scales, and are hence still less viscous overall. Incidentally, the run without a shear viscosity limiter (S3-tav) agrees well with the result of Price (2012) for his 128^3 run with time-variable viscosity (shown also in the figure, for comparison), except on small scales due to Price’s choice of measuring the power spectrum of the SPH-smoothed velocity field. However, the 256^3 result of Price (2012) with matching resolution lies still a bit higher, similar to our S3 result with $\alpha = 0.01$. This is presumably caused by small differences in how the time-dependent viscosity is parameterized.

3.6 Reynolds numbers

In a response paper to our original submission the present work, Price (2012) argued that our SPH results for subsonic turbulence can be naturally explained simply by our artificial viscosity settings. In fact, he suggests that SPH effectively yields a solution of

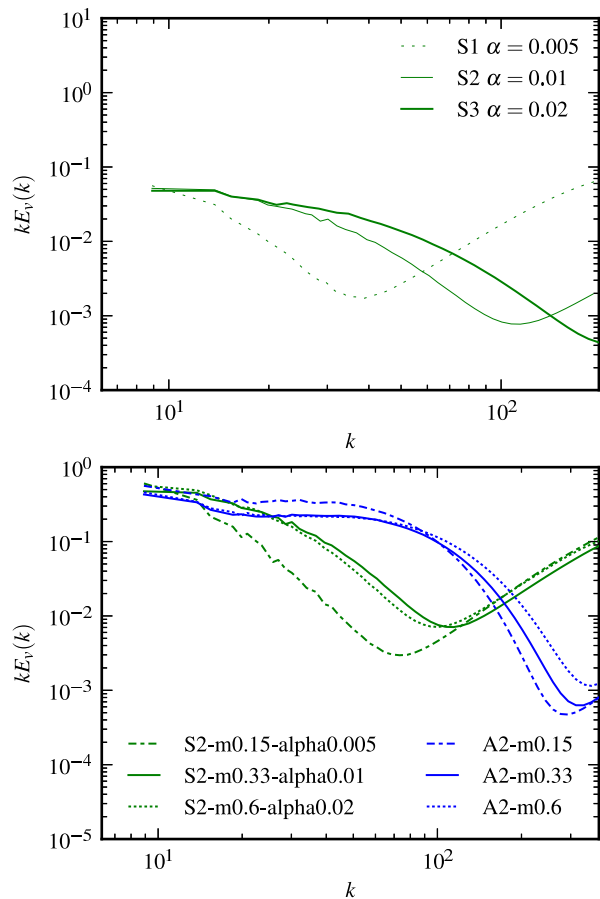


Figure 10. Velocity power spectra in SPH for different numerical settings but equal Reynolds numbers. In the top panel, we compare results for different numerical resolutions, ranging from 64^3 (S1) to 256^3 (S3), and different artificial viscosity settings, such that the Reynolds number estimated according to equation (17) is the same and a very similar result would in principle be expected. In the bottom panel, we show instead results at a fixed resolution of 128^3 (S2), but here the Mach number is varied and the viscosity parameter is adjusted such that the estimated Reynolds number stays the same. An approximate self-similarity of the spectral shape is at best obtained only for large Mach numbers. For comparison, we also show corresponding results for different Mach numbers for the moving-mesh code. Here the dynamic range of the inertial range is to a good approximation set by the grid resolution and is invariant with the Mach number.

the Navier-Stokes equation with a kinematic viscosity ν that can be estimated as

$$\nu \simeq \frac{1}{10} \alpha v_{\text{sig}} h, \quad (16)$$

where α is the artificial viscosity coefficient, $v_{\text{sig}} \simeq c_s$ is the signal velocity, and h is the SPH smoothing length. He further argues that the Reynolds number of the SPH turbulence simulations is then given by

$$\mathcal{R}_e \equiv \frac{LV}{\nu} = \frac{10L}{\alpha h} \mathcal{M}. \quad (17)$$

Adopting as characteristic velocity scale the *rms*-velocity of the turbulent velocity field (i.e. $V = \mathcal{M}c_s$), and for the length scale L the box size, Price (2012) estimates a Reynolds numbers of $\mathcal{R}_e \simeq 6000$ for his 256^3 run. He also claims that “turbulent flow with a Kolmogorov spectrum can be easily recovered” in SPH when α

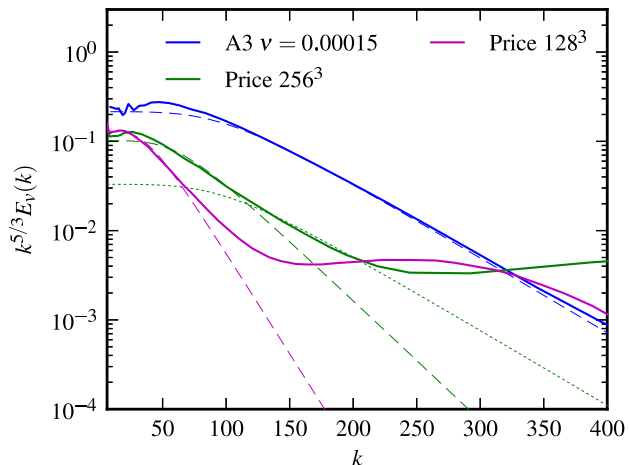


Figure 11. Shape of the dissipation range in a moving-mesh simulation with physical viscosity, and in the SPH subsonic turbulence simulations of Price (2012). The dashed lines show fits to the velocity power spectrum based on equation (18), corresponding to Reynolds numbers 2100, 1000 and 540 for AREPO and the 256^3 and 128^3 SPH results, respectively. The green dotted line is the expected shape for $\mathcal{R}_e = 2100$ turbulence, shifted in amplitude to fit part of the SPH result with 256^3 particles. It is clear that the dissipation range of the SPH results is not consistent in detail with a Kolmogorov cascade. We note that Price (2012) quotes a Reynolds number of 6000 for his 256^3 result.

is reduced away from shocks, and that our argument that gradient errors are responsible for a flawed Kolmogorov cascade would be “incorrect”.

Actually, it is these assertions that are incorrect, as we show now. If the Reynolds number of SPH was indeed simply given by equation (17) as suggested by Price (2012), we would expect *invariant* results (in the sense of Reynolds-number similarity) for the turbulent power spectrum in different simulations when the Reynolds number and the driving are kept constant. This is however not the case, as is shown in Figure 10. Here we compare in the top panel a series of different SPH simulations in which the resolution is progressively increased by factors of 2, and the viscosity parameter α is correspondingly changed such that the (estimated) kinematic viscosity and Reynolds number stay fixed in all cases. Nevertheless the numerical results for SPH do not line up. In the bottom panel of Fig. 10, we vary the Mach number of the turbulence at fixed resolution, again adopting different viscosity settings such that the Reynolds number according to equation (17) should stay the same. Again, an accurate universality of the shape of the SPH turbulence is not recovered, although there is a hint that this may work better for large Mach numbers.

Another important point to make is that not only the inertial range of Kolmogorov turbulence for a Navier-Stokes flow is universal, the dissipation range is universal as well (e.g. Pope 2000). In fact, experiments demonstrate that the energy spectrum can be well described by

$$E(k) = C \epsilon^{2/3} k^{-5/3} f_\eta(k\eta), \quad (18)$$

where ϵ is the dissipation rate, and

$$\eta \equiv \left(\frac{\nu^3}{\epsilon} \right)^{1/4} \quad (19)$$

is the Kolmogorov scale. The function $f_\eta(x)$ is universal and well

fit by

$$f_\eta(x) = \exp\left(-\beta[(x^4 + c^4)^{1/4} - c]\right), \quad (20)$$

with $c \sim 0.4$ and $\beta \sim 5.2$, and the value of the Kolmogorov constant, $C \sim 0.5$, is universal as well. Note that this means that for quasi-stationary turbulence, where the energy injection rate is equal to the dissipation rate, not only the inertial range is specified but also the shape of the spectrum in the dissipation range is fully specified if the kinematic viscosity is known.

In Figure 11, we plot the velocity power spectra for the 256^3 and 128^3 SPH runs of Price (2012), and we compare them to a run with our Navier-Stokes solver in AREPO (Muñoz et al. 2012), with $\nu = 0.00015$ at a resolution of 256^3 cells. The expected Reynolds number of this mesh-based simulation with prescribed physical viscosity (physical + numerical viscosity) is $\mathcal{R}_e \sim 2100$. By plotting the spectrum using a linear scale for k , the dissipation range is emphasized and becomes approximately a straight line. We readily see that AREPO provides an excellent fit to the expected shape (dashed line), as described by equations (18) and (20), only a small deviation due to the bottleneck bump is present. However, neither the 128^3 nor the 256^3 SPH results of Price (2012) provide a reasonable fit to the shape expected for Kolmogorov turbulence in the dissipation range. This invalidates the claim that the subsonic turbulence results of Price (2012) (which are quite consistent with our own for the similar viscosity settings, see Fig. 9) are consistent with Kolmogorov turbulence. It also shows that the Reynolds numbers quoted by Price (2012) are incorrect and too high by a factor of ~ 6 ; in fact, his 256^3 run has at most $\mathcal{R}_e \sim 1000$, and the 128^3 run about half that, but since the results do not accurately correspond to the expected Navier-Stokes solutions for these Reynolds numbers, these values have to be taken in any case with a grain of salt. We also want to remark that the dynamic range expected for the inertial range of Kolmogorov turbulence is of order $\eta/L \sim \mathcal{R}_e^{-3/4}$. A Reynolds number of 6000 should hence allow up to $\eta/L \sim 680$ – clearly infeasible with 256 points per dimension.

Finally, we turn to the issue of gradient errors in SPH, which according to Price (2012) play no role in the turbulence results. To examine this point, we carry out a simple experiment of a decaying large scale solenoidal velocity field. We set up a simple random realization of a number of solenoidal velocity modes on large scales (the largest 70 k -modes in the box), with a $\propto k^{-5/3}$ energy spectrum and normalized such that the resulting *rms*-velocity corresponds exactly to a $\mathcal{M} = 0.3$ Mach number. We now compare the time evolution of this field in three different simulations, without applying any driving. We expect that the large-scale shearing motions in the initial conditions will transfer some of their energy to smaller scales with time, and that the damping of these motions by numerical viscosity effects will eventually dissipate the kinetic energy of the system. One of the three codes we try is our moving-mesh code AREPO. The second is standard SPH with a low viscosity setting of $\alpha = 0.01$. The third simulation uses the very same SPH code, but with the only difference being that the pressure in the equation of motion is replaced by $P \rightarrow P - P_0$, where the constant $P_0 = \rho_0 c_s^2$ is taken to be the background pressure. In principle, such a constant pressure offset should not change anything, as pressure gradients are unaffected and hence no effect on the dynamics is expected. However, SPH's equation of motion has a 'zeroth-order' error in the pressure gradient which is proportional to the pressure itself (e.g. Quinlan et al. 2006; Read et al. 2010; Gaburov & Nitadori 2011; Amicarella et al. 2011). For example, Read et al. (2010) show that the actual acceleration acting on a

SPH particle corresponds to

$$\frac{d\mathbf{v}_i}{dt} = -\frac{P_i}{h\rho_i}\mathbf{E}_{0,i} - \frac{(\mathbf{V}_i\nabla_i)P_i}{\rho_i} + \mathcal{O}(h), \quad (21)$$

where $\mathbf{E}_{0,i}$ is a dimensionless error vector, and \mathbf{V}_i is a dimensionless error matrix. Only for $\mathbf{E}_{0,i} = 0$ and \mathbf{V}_i equal to the identity matrix the correct equation of motion would be obtained. For an irregular particle distribution, one obtains however $\mathbf{E}_{0,i} \sim \mathcal{O}(h)$, meaning that the zeroth-order error is not easily reduced with better resolution. However, by subtracting P_0 , the average pressure of a particle is made close to zero, and with this trick the magnitude of the zeroth-order error should be greatly reduced.

Indeed, if we look at the time evolution of the power spectrum of our decaying velocity field (Figure 12), we see a substantial difference between the two flavours of SPH. The standard version of SPH builds up small-scale velocity noise much more quickly, and the power on large scales decays more rapidly as well. In contrast, the version of SPH with a pressure-bias in the equation of state manages to track the AREPO result on large scales for a much longer time. This hence proves that the small-scale noise created by gradient errors drains kinetic energy from large scales, effectively short-circuiting the Kolmogorov cascade. Notice that the two flavours of SPH examined here have identical viscosity settings, i.e. their only difference lies in the gradient errors in the SPH equation of motion. Unfortunately, in general applications of SPH in astrophysics the subtraction of a constant background pressure is not readily possible, so the problem of gradient errors is present irrespective of the artificial viscosity settings.

We note that the problematic influence of noise and gradient errors in SPH has also become apparent in recent tests of the Gresho vortex problem (Springel 2010; Read & Hayfield 2011). The stable vortex flow in this set-up (Gresho & Chan 1990) tends to decay relatively quickly in standard SPH, but Read & Hayfield (2011) recently showed that the error and the convergence rate can be greatly improved if a higher-order gradient estimate, based on a much larger number of SPH smoothing neighbours and a different kernel shape, is used.

It is also interesting to consider the computational cost required to reach a certain effective Reynolds number in SPH and in a mesh scheme. If we ignore the issue of gradient errors in SPH for the moment and assume that the Reynolds number is indeed given by equation (17), then the computational cost to reach a certain Reynolds number scales as $t_{\text{CPU}} \propto \mathcal{R}_e^4$. This is because the number of particles scales as h^{-3} , and the number of required timesteps as h^{-1} . In contrast, because in a mesh code such as AREPO the Kolmogorov dissipation scale is essentially given by the cell size, $\eta \sim h$, we expect $\mathcal{R}_e \propto h^{-4/3}$, implying that the required CPU-time to reach a certain Reynolds number scales only as $t_{\text{CPU}} \propto \mathcal{R}_e^3$. In the limit of large Reynolds numbers this is a significant competitive advantage.

3.7 Vorticity power spectrum

Another interesting probe for turbulence is provided by the vorticity $\boldsymbol{\omega} = \nabla \times \mathbf{v}$ of the velocity field. This is because vorticity is in principle a conserved fluid quantity in an ideal gas, where the vorticity field is locked into the gas similar to a flux-frozen magnetic field in ideal magnetohydrodynamics. New vorticity is introduced on large scales through our solenoidal driving field, and it is erased on small scales via dissipation, but vorticity production through the baroclinic term should essentially be absent in our flow due to our quasi-isothermal conditions. Analyzing the statistical properties of

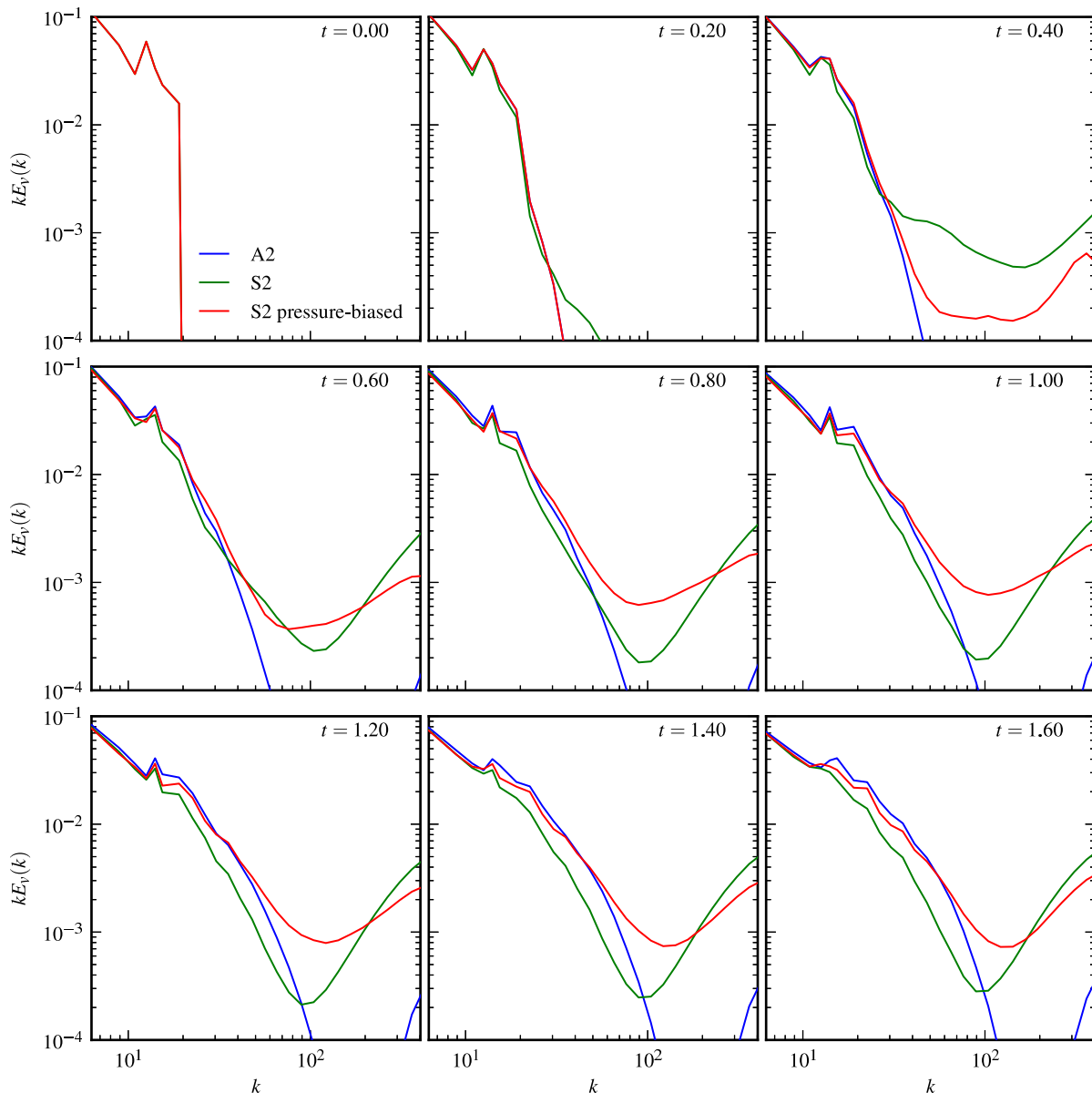


Figure 12. Time evolution of the velocity power spectrum of a decaying large-scale solenoidal velocity field. Initially, only the ~ 70 largest modes are populated with random phases and an expected $E(k) \propto k^{-5/3}$ energy spectrum, normalized such that the *rms* velocity corresponds to $\mathcal{M} = 0.3$. We compare three different simulation techniques: AREPO (blue), ordinary SPH (green) with a low viscosity of $\alpha = 0.01$, and “pressure-biased” SPH (red), where the only difference is that a constant pressure $P_0 = \rho_0 c_s^2$ is subtracted in the equation of state. The resolution is 128^3 in all cases. We see that ordinary SPH builds up small-scale noise considerably more quickly than the pressure-biased version of SPH. The latter actually tracks the AREPO result on large and intermediate scales much longer than ordinary SPH. As the viscosity in both SPH versions is the same, the faster dissipation of the large-scale motions in ordinary SPH is due to the larger noise on the smallest scales, as the energy dissipation rate $E_{\text{diss}}(k) \propto k^2 E(k)$ is dominated by these scales.

the vorticity field can hence provide complementary information about turbulence and the numerical properties of the employed simulation technique.

In Figure 13, we show our measurements for the vorticity power spectrum for the same simulations that we used in Fig. 5 for an analysis of the velocity power spectrum. Both our moving-mesh and fixed-mesh simulations show approximately a power-law rise of the vorticity with scale, until a rapid drop sets in at around the numerical dissipation scale. For fully developed isotropic turbulence we expect a power-law spectrum of the vorticity given by $E_w \simeq k^2 E_v$ (e.g. Zhu et al. 2010). In particular, Kolmogorov’s

theory then suggests a slope that is 2 units shallower than that of the velocity spectrum, and hence rises towards smaller scales as $E_w \propto k^{1/3}$. This expectation is borne out well by our measurements, providing an important consistency check. Also, the proportionality between E_w and $k^2 E_v$ is resolved quite well, as shown by the dashed lines.

However, as already expected based on the enstrophy maps shown in Fig. 4, the SPH results for the vorticity power spectrum are very different. In essence, only some large eddies resulting from the driving are present, apart from some vorticity power on small scales, which is likely in large part noise, and in any case is smaller

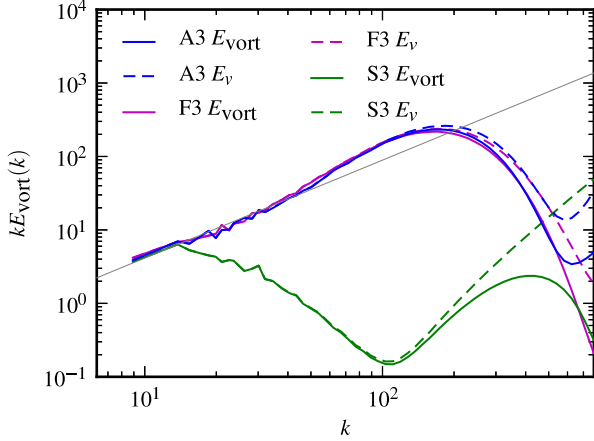


Figure 13. Vorticity power spectrum of SPH and AREPO, compared at a resolution of 256^3 . The thin grey line gives the slope expected for Kolmogorov’s theory of incompressible turbulence, in which for fully developed turbulence, the power spectrum of the vorticity is proportional to k^2 times the velocity power spectrum. The AREPO result follows this expectation very well on large scales, over the same range where also Kolmogorov’s velocity power spectrum is reproduced. In contrast, SPH shows a rapid fall of vorticity towards small scales; only on scales of order the SPH smoothing length a substantial vorticity bump is seen, but this is presumably largely due to the velocity noise on these scales.

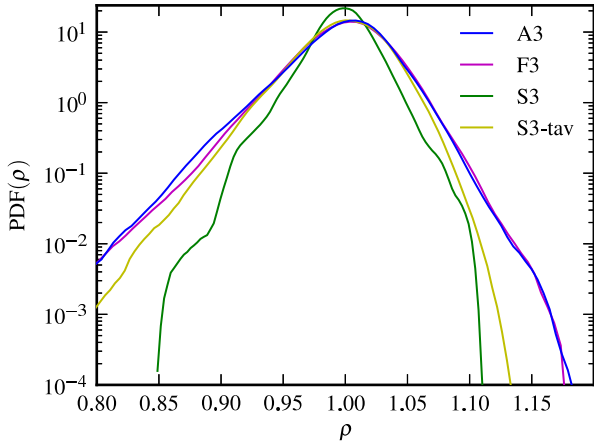


Figure 14. Volume-weighted density PDFs for subsonic turbulence. Shown are SPH, AREPO, and fixed-mesh simulations. The PDFs are averaged over 5 snapshots taken at times $t = 12.8, 16.0, 19.2, 22.4$ and 25.6 .

than what is found in the mesh code. This hence corroborates our previous results, confirming that the mesh-based simulations do resolve subsonic turbulence with the expected physical properties whereas this is more problematic in the case of SPH.

3.8 Density probability distribution function

The final quantity we examine in our simulations of subsonic turbulence is the density distribution function. In Figure 14, we compare the volume-weighted density PDFs for our A3, F3, S3, and S3-tav simulations. These distribution functions have been averaged over 5 simulation snapshots evenly spaced in time between $t = 12.8$ and $t = 25.6$ since the start of the simulations.

We find that the mesh codes agree well in their density PDF. However, the AREPO code in moving-mesh mode shows slightly more high-density regions than when a fixed-mesh is used. This is consistent with our expectation that the moving mesh yields a slightly lower numerical viscosity and a better adaptivity to high density regions. Due to the subsonic conditions in these simulations, the differences are expected to be quite small though. The density PDF of the SPH simulation shows somewhat larger differences. The comparatively viscous $\alpha = 1.0$ result is slightly thinner and hence more strongly peaked towards the mean value than for the mesh-based results. This is despite the fact that noise in the SPH density estimates can be expected to broaden the intrinsic distribution, but apparently this effect is negligible compared to the physical width of the distribution one expects for $\mathcal{M} \sim 0.3$ turbulence. Interestingly, our SPH run with time-variable artificial viscosity produces a density PDF very close to the mesh-based results on the low-density side, whereas it falls short a bit in the tail of the high-density side.

4 TRANSSONIC AND SUPERSONIC TURBULENCE

Superficially, the results obtained thus far seem to be in conflict with previous reports that SPH can adequately represent highly supersonic isothermal turbulence. However, it is important to appreciate that the physical nature of supersonic isothermal turbulence is really quite different from the subsonic regime studied thus far, both in terms of the role of ram pressure versus thermal pressure, and in terms of the relevant dissipation mechanisms. In supersonic turbulence, we expect a network of shocks, which in the limiting case of fully kinetic turbulence is described by Burgers turbulence and not by the Kolmogorov theory.

We here briefly examine how well our new moving-mesh code AREPO describes turbulence in the transsonic and highly supersonic regimes, and whether the SPH results improve in this regime. The names and key parameters of the primary simulations we have carried out for these tests are listed in Table 3. A first impression is obtained by the maps in Figure 15, where we show slices through the density and kinetic energy density fields in our $\mathcal{M} = 8.4$ simulations using a moving mesh in AREPO, a fixed mesh, or SPH. Right away we notice a much greater similarity of the maps than found in the subsonic regime, with SPH apparently being able to resolve the turbulence in a way that is at least qualitatively similar to the mesh-based results.

We examine this more quantitatively in Figure 16, where we show the velocity and density power spectra for increasing Mach numbers, ranging from the transsonic to the supersonic regime. We include results for all three types of numerical simulations that we have carried out, comparing them always with an identical forcing field as a function of time.

The simulations shown in Fig. 16 were performed for Mach numbers $\mathcal{M} \sim 1.2$ (top row), $\mathcal{M} \sim 3.5$ (middle row) and $\mathcal{M} \sim 8.4$ (bottom row). We clearly see that as the Mach number increases, the SPH method does progressively better for the velocity power spectrum and in fact appears to eventually converge to the result obtained with the two mesh-based techniques. While for $\mathcal{M} \sim 1.2$, there is still a very significant deficit of power in SPH except for the largest scales, this effect becomes significantly weaker for $\mathcal{M} \sim 3.5$ and almost vanishes for $\mathcal{M} \sim 8.4$. When one compares the velocity power spectra of the moving-mesh and the fixed-mesh calculations, one generally finds very good agreement on large scales but a noticeable difference in the small-scale

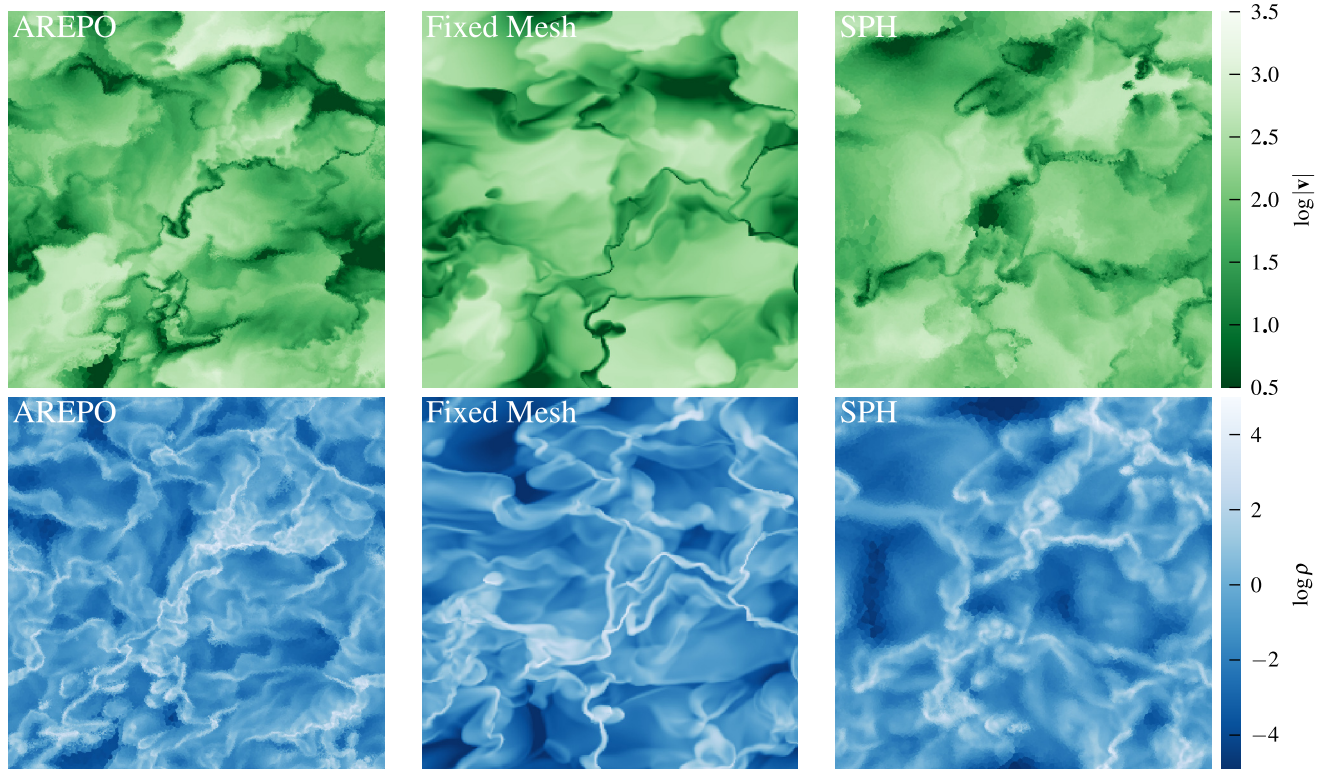


Figure 15. Visualizations of the state of the gas in slices through our $\mathcal{M} \sim 8.4$ supersonic runs at 256^3 resolution. The top row shows the logarithm of the velocity field and the bottom row the logarithm of the density field. From left to right, simulations with a moving mesh in AREPO (A3-m10), a fixed mesh (F3-m10), and SPH (S3-m10) are shown.

behaviour. The dissipation scale of the moving-mesh code lies at slightly smaller scale, which can be interpreted as a signature of a higher effective resolution for the same number of fluid cells. This advantage most likely arises from the reduced advection errors in the moving-mesh approach.

If instead the density power spectra are compared (right column in Fig. 16), we find a qualitatively similar behaviour. For higher Mach number, the SPH result approaches that of the mesh-based simulations. There are however somewhat larger residual differences between all three techniques at the highest Mach number compared with the situation found for the velocity power spectrum. In particular, the density power spectrum for the moving-mesh code has a shallower slope and extends to higher k than both for the fixed-mesh and the SPH codes. We interpret this as a result of the better adaptive resolution of the moving-mesh technique. Direct fits to the power-law region of the density power spectra at $\mathcal{M} \sim 8.4$ return slopes of -0.54 and -0.43 for these 256^3 moving-mesh and SPH runs, respectively, clearly indicating a significant difference. However, we note that the shape of the density power spectrum is relatively sensitive to resolution, as we show next, so these slopes are not numerically converged.

In Figure 17, we show a resolution study for our moving-mesh and fixed-mesh simulations for the cases of $\mathcal{M} \sim 3.5$ and $\mathcal{M} \sim 8.4$ turbulence, considering results both for the velocity and density power spectra. It is seen that the velocity power spectra agree nicely between the moving-mesh and the fixed-mesh code at large scales, but that the effective resolution of the moving-mesh code is higher at a given number of resolution elements. When the resolution is

improved, the power-law region corresponding to the inertial range is extended towards smaller scales, without a significant change in slope. A small bottleneck effect still seems to be present, but at a much smaller level than in the subsonic regime.

In contrast, convergence in the density power spectrum is more challenging, as seen in the right column panels of Fig. 17. Here low resolution can easily lead to an overestimate of the slope due to a fairly prominent bottleneck effect. Interestingly, in the $\mathcal{M} = 8.4$ case we see that the slope of the fixed-mesh F4-m10 simulation is accurately reproduced already by the A3-m10 simulation, at an almost one order of magnitude smaller number of resolution elements, and similarly for the F3-m10 and A2-m10 pair of simulations. This can be attributed to the adaptive nature and the lower advection errors of the moving-mesh approach compared with the fixed-grid Eulerian method.

It is also interesting to examine the energy dissipation power spectra of the different simulation techniques in the highly supersonic regime. This is done for our highest Mach number run in Figure 18. All the simulations show a relatively broad distribution of dissipation as a function of scale, which is quite different in character compared to the narrower distribution encountered in the subsonic case. This can be interpreted as a result of the different physical nature of the dissipation in this supersonic regime, which occurs primarily through a complex network of shock surfaces, and is hence not restricted to a small range of length scales. It is also interesting to note that SPH and the moving-mesh code show quantitatively a quite similar result, whereas the fixed-mesh method gives higher dissipation on nearly all scales. We argue that this is due

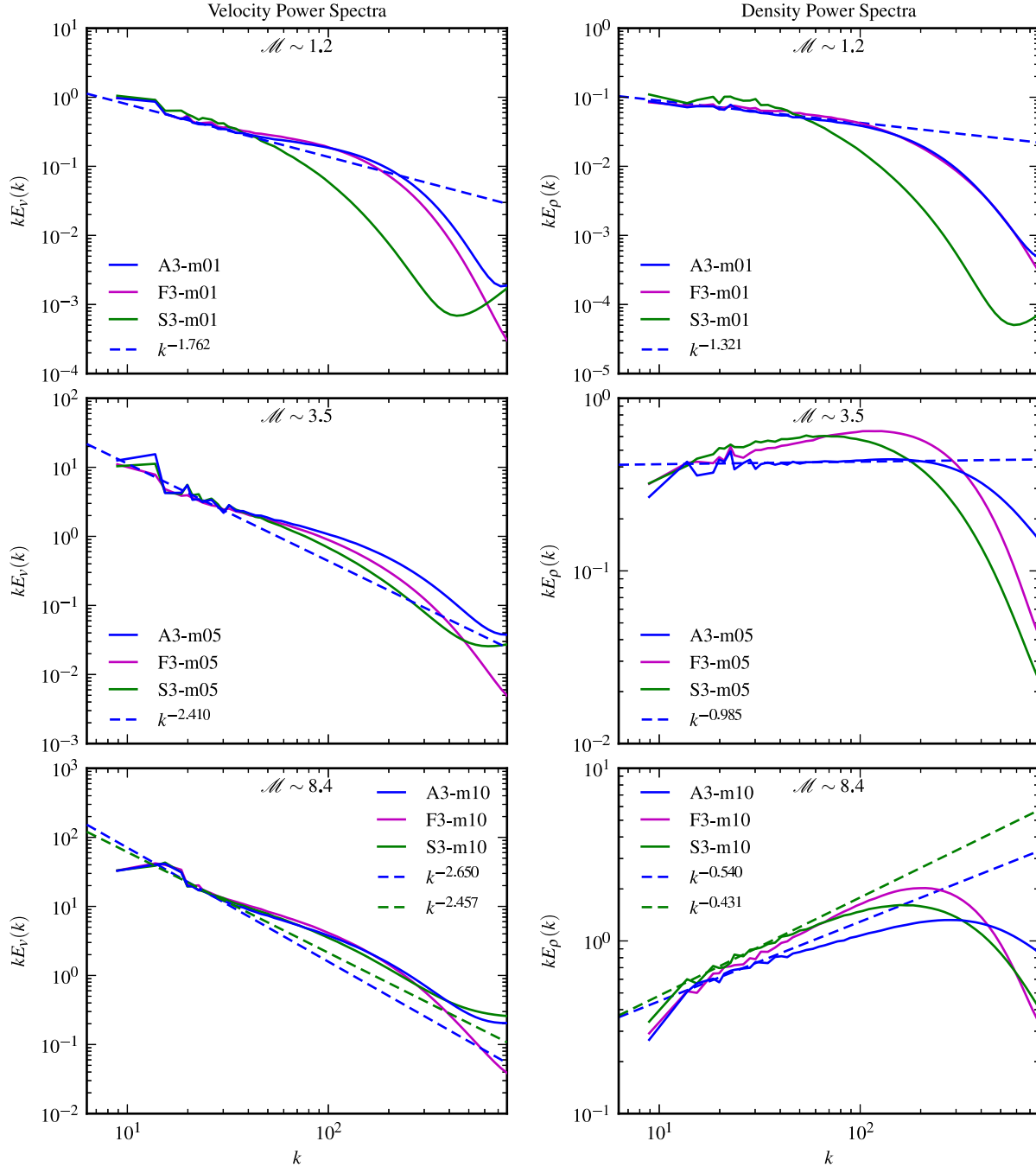


Figure 16. Turbulence power spectra of SPH, AREPO, and a fixed-mesh code for approximately sonic (top panel), mildly supersonic (middle panel) and for highly supersonic driven isothermal turbulence (bottom panel). The left panels show the velocity power spectra, the right panels the density power spectra. The dashed lines show fitted power-laws for AREPO (blue) and SPH (green).

to the significant bulk motion present in the system, inducing enhanced dissipation through advection errors in the fixed-mesh code. This is simply not present in this form in the two Lagrangian methods, which are both Galilean-invariant schemes.

Finally, Figure 19 takes a look at the volume-weighted density probability distribution function (PDF) in the high Mach number case. We compare the PDFs of moving-mesh, fixed-mesh and SPH simulations at the 256^3 resolution. The shape of all three results is described reasonably well by a log-normal distribution. However,

the fixed-mesh simulation shows a higher probability at the low density end and has the largest width of the distribution for this reason. The SPH simulation tends to give higher probability at the high density end, which is a very similar behaviour as found in Price & Federrath (2010). The moving-mesh run has an overall very similar distribution as the SPH run, except for being slightly wider. To the extent that a better representation of the high-density tail is advantageous in science applications of supersonic turbulence (which can be argued is particularly true in studies of star formation), the

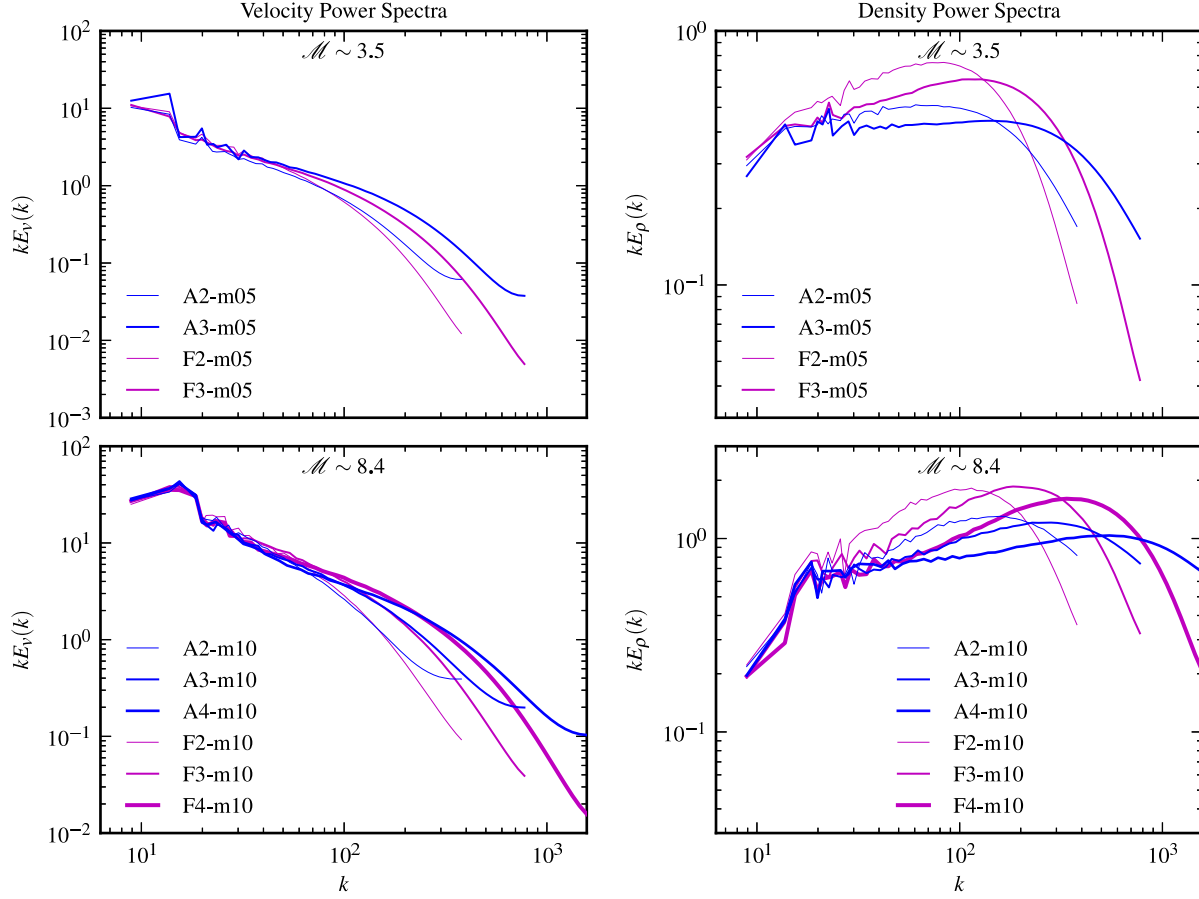


Figure 17. Resolution study of the supersonic velocity and density power spectra for our fixed-mesh and moving-mesh simulations. The top panels show the runs at Mach number $\mathcal{M} \sim 3.5$, and the bottom ones at $\mathcal{M} \sim 8.4$. At large and intermediate scales, the moving-mesh runs correspond roughly to the fixed-mesh runs at 2^3 times higher resolution.

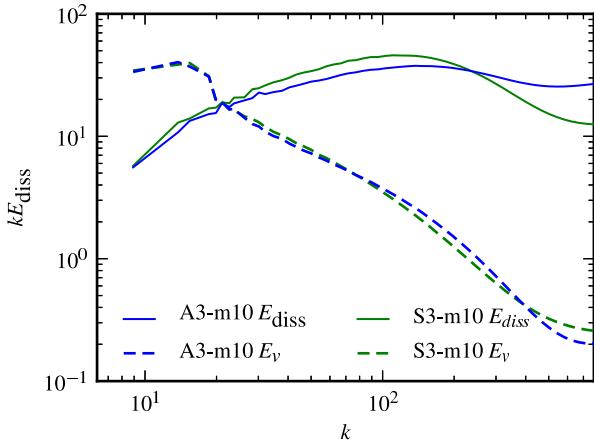


Figure 18. Dissipation power spectra for the supersonic runs A3-m10, F3-m10 and S3-m10 at $\mathcal{M} \sim 8.4$. As in Fig. 7 the velocity power spectra are plotted as dashed lines.

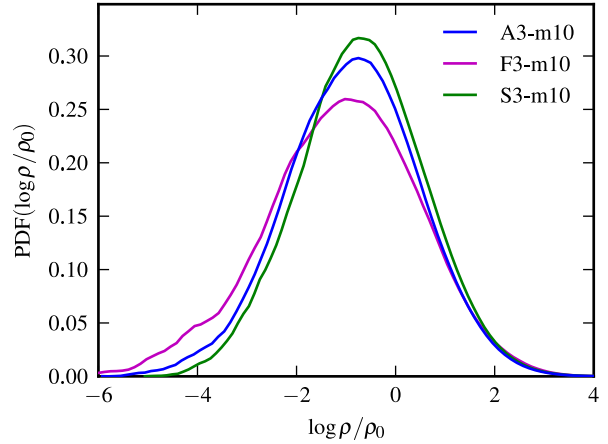


Figure 19. The volume-weighted logarithmic density PDFs for our highly supersonic runs at $\mathcal{M} \sim 8.4$, as labeled. The PDF is averaged over two snapshots at times $t = 0.2$ and $t = 0.3$.

5 DISCUSSION AND CONCLUSIONS

moving-mesh technique hence works at least as well as SPH, and arguably better than a fixed-mesh technique.

Perhaps the most important question prompted by our results is why SPH behaves so badly in the subsonic regime. Price (2012)

argued that the culprit lies simply in the artificial viscosity parameterization, and that schemes that dynamically reduce the viscosity away from shocks (e.g. Morris 1997; Dolag et al. 2005; Cullen & Dehnen 2010) do much better and have no problem to reproduce a Kolmogorov cascade also in the subsonic regime. While we agree that excessive artificial viscosity can compromise the results of SPH, particularly in the subsonic regime where this will show up more readily, this is by no means the complete story. Instead, we have demonstrated in this study that gradient errors inherent in standard formulations of SPH (‘classic SPH’) do play a major role as well. They seed small-scale velocity noise in shear flows on all scales, and this noise is dissipated away by the viscosity of the scheme. Since SPH is an energy-conserving scheme, this effectively short-circuits part of the energy transfer cascade in Kolmogorov’s theory of turbulence.

The concern that the large subsonic noise in SPH may cause substantial accuracy problems in the treatment of fluid instabilities has recently been emphasized by a number of authors (Springel 2010; Read et al. 2010; Abel 2011). Also, numerous studies have pointed out that the standard approach followed in SPH for constructing derivatives of smoothed fluid quantities involves rather large error terms, especially for the comparatively irregular particle distributions in multi-dimensional simulations. One problem lies in a lack of consistency of the ordinary density estimates (which do not conserve volume, i.e. the sum of m_i/ρ_i is not guaranteed to add up to the total volume), and another in a low order of the gradient estimate itself (e.g. Quinlan et al. 2006; Read et al. 2010; Gaburov & Nitadori 2011; Amicarella et al. 2011). In practice, this means that there can be pressure forces on particles even though all individual pressure values of the particles are equal, a point emphasized in a recent study by Abel (2011). But if this is the case, spurious jittering motions of particles can be readily triggered even for a vanishingly small large-scale pressure gradient.

In order to demonstrate this point explicitly and quantify the typical noise in the pressure gradient estimates of SPH and AREPO, we have carried out a simple experiment. To this end we used the particle coordinates \mathbf{x}_i of the last snapshot of our S3 subsonic simulation run, which is representative for the particle distribution typically encountered in SPH in this situation. We then assigned entropies to the particles (taking their density estimate into account) such that the pressures $P_i = P(\mathbf{x}_i)$ of individual particles were given by the analytic pressure profile

$$P(\mathbf{x}) = P_0 \mathbf{q} \cdot \mathbf{x} + r, \quad (22)$$

which is a simple linear gradient in the \mathbf{q} -direction (our results are independent of the actual orientation of this vector) with a constant pressure offset r . The SPH estimate for the pressure gradient was then inferred from the particle acceleration \mathbf{a}_{SPH} computed by the SPH code as

$$\nabla P = -\mathbf{a}_{\text{SPH}} \rho, \quad (23)$$

which is the relevant quantity that ultimately enters the discretized equation of motion. We can then consider the relative error of these SPH pressure gradient estimates with respect to the known analytic gradient. We define the corresponding errors as

$$e_{\text{rel}} = \frac{|\nabla P - P_0 \mathbf{q}|}{|P_0 \mathbf{q}|}, \quad e_\varphi = \frac{\mathbf{q} \cdot \nabla P}{|\mathbf{q}| |\nabla P|} = \cos \phi, \quad (24)$$

and show them as scatter plots for a random subset of the points in Figure 20.

For comparison, we also carried out the equivalent procedure for the AREPO code, based on the same particle coordinates. The

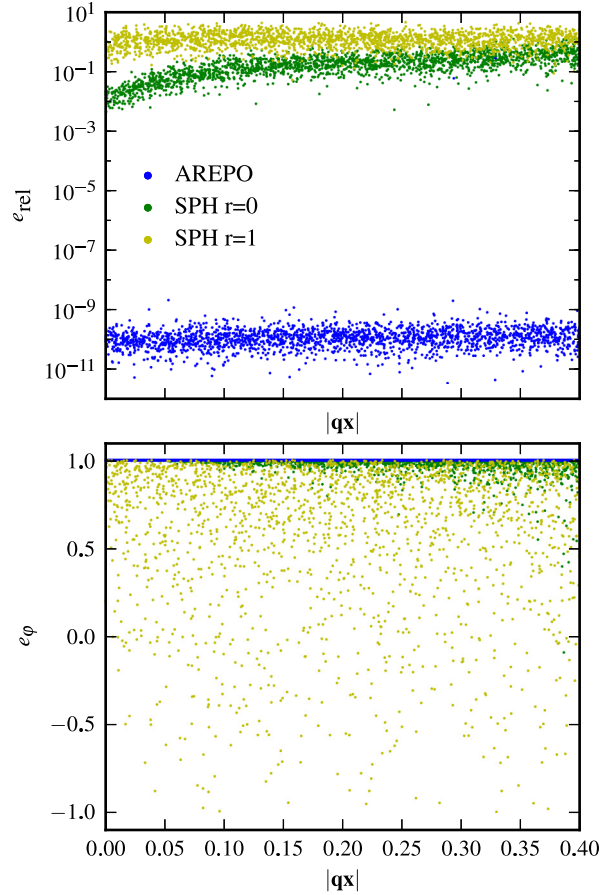


Figure 20. The top panel shows a scatter plot of the relative errors of pressure gradient estimates in a simple test set-up. The bottom panel shows the corresponding errors in the direction of the estimated pressure gradients. The errors of AREPO are at the level of machine precision. However, SPH shows severe errors in the pressure gradient estimates, with a size that depends on the magnitude of the pressure itself. If a constant offset of $r = 1$ is added to the pressure profile, the gradient errors are about ten times larger, exceeding even 100%.

resulting errors are also shown in Figure 20. AREPO clearly calculates the pressure gradients highly accurately, both in magnitude and angle. In fact, AREPO’s gradient estimate is second-order accurate, independent of the distribution of points (Springel 2010), implying that a linear gradient should be reproduced essentially to machine precision, which we find is also the case here. In contrast, SPH shows a huge scatter in both error measures. In fact, the magnitude of the absolute error can in extreme cases be up to twice as large as the value of the gradient itself, and also the angular errors are significant. Furthermore, the errors rise with the magnitude of p . If a pressure offset $r = 1$ is added to the pressure profile, the relative error is increased by about an order of magnitude, which can be understood in terms of a higher E_0 error in equation (21). We have also repeated the calculation for increased numbers of neighbours, which reduces the error, albeit only weakly. We note that these large errors occur for a rather simple problem – a spatially constant gradient. This makes it clear that standard SPH has comparatively low-order accuracy for smooth flow.

We thus think that the problems of SPH in resolving subsonic turbulence are serious. It is unlikely that they can be solved by

just increasing the resolution, reducing the artificial viscosity, or the number of smoothing neighbours. This is because changing the artificial viscosity parameterization does not improve the gradient estimates, and will hence not be able to resolve the underlying problem. Furthermore, obtaining better gradient estimates through a larger number of SPH smoothing neighbours is efficiently blocked by the clumping instability, at least for the ordinary kernel of classic SPH. In any case, what appears to be needed for better results in the subsonic regime are better gradient estimates. Some extensions and improvements of the standard SPH formulation that go into this direction have already been proposed (e.g. Price 2008; Heß & Springel 2010; Cullen & Dehnen 2010; Read et al. 2010; Read & Hayfield 2011; Abel 2011). It will remain to be seen whether any of them provides a robust and generally applicable alternative to standard SPH.

We should clarify that despite the large errors in gradient estimates, it remains true that SPH has very good conservative properties. This feature allows it to still produce physically sensible fluid behaviour in many situations despite the subsonic noise, especially in shock-dominated regimes where the accuracy of gradient estimates is much less important. Our results hence justify the application of standard SPH in studies of supersonic turbulence, provided the Mach number is really high. At the same time, our results raise significant concerns for applications of SPH in regimes where subsonic phenomena such as turbulence are important. This is for example expected to be the case in cosmological structure formation. Indeed, recent studies have already presented evidence that the accuracy problems of SPH in the treatment of the generation of turbulence and of fluid instabilities such as the Kelvin-Helmholtz instability affect galaxy formation directly (Vogelsberger et al. 2011; Keres et al. 2011; Sijacki et al. 2011).

Another important conclusion from our results is that the new moving-mesh code AREPO is highly competitive with the accuracy of ordinary Eulerian mesh-codes for studies of turbulence. In the subsonic regime it produces essentially equivalent results as ordinary Eulerian codes, with a slightly reduced dissipativeness of the scheme. In the supersonic regime it however features a higher effective resolution at the same number of resolution elements. In particular, the velocity and density power spectra can be traced to smaller scales, and there is generally less dissipation as a function of scale due to reduced advection errors. If just pure hydrodynamics without self gravity is considered, a moving-mesh calculation with AREPO is however more costly than a corresponding fixed-mesh or SPH calculation with the same number of resolution elements. It is clear that an accurate description of turbulent gas motions is highly desirable for a versatile astrophysical code, and we have shown here that AREPO is able to meet these requirements.

ACKNOWLEDGEMENTS

We would like to thank Christoph Federrath and Daniel Price for their turbulent driving routine, which we have incorporated in modified form in our AREPO and GADGET-3 codes. We would also like to thank Christoph Federrath, Dusan Keres, Mordecai-Mark Mac Low, Colin McNally for very insightful comments. AB gratefully acknowledges financial support from the Klaus Tschira Foundation, and VS from DFG Research Center SFB 881, ‘The Milky Way System’.

REFERENCES

- Abel T., 2011, *MNRAS*, 413, 271
- Agertz O., Moore B., Stadel J., Potter D., Miniati F., Read J., Mayer L., Gawryszczak A., Kravtsov A., Nordlund Å., Pearce F., Quilis V., Rudd D., Springel V., Stone J., Tasker E., Teyssier R., Wadsley J., Walder R., 2007, *MNRAS*, 380, 963
- Amicarelli A., Marongiu J., Leboeuf F., Leduc J., Neuhauser M., Fang L., Caro J., 2011, *International Journal for Numerical Methods in Engineering*, 87, 677
- Ballesteros-Paredes J., Gazol A., Kim J., Klessen R. S., Jappsen A.-K., Tejero E., 2006, *ApJ*, 637, 384
- Balsara D. S., 1995, *J. Comp. Phys.*, 121, 357
- Cullen L., Dehnen W., 2010, *MNRAS*, 408, 669
- Dolag K., Vazza F., Brunetti G., Tormen G., 2005, *MNRAS*, 364, 753
- Federrath C., Klessen R. S., Schmidt W., 2008, *ApJ*, 688, L79
- Federrath C., Klessen R. S., Schmidt W., 2009, *ApJ*, 692, 364
- Federrath C., Roman-Duval J., Klessen R. S., Schmidt W., Mac Low M.-M., 2010, *A&A*, 512, A81
- Gaburov E., Nitadori K., 2011, *MNRAS*, 414, 129
- Greif T. H., Springel V., White S. D. M., Glover S. C. O., Clark P. C., Smith R. J., Klessen R. S., Bromm V., 2011, *ApJ*, 737, 75
- Gresho P. M., Chan S. T., 1990, *International Journal for Numerical Methods in Fluids*, 11, 621
- Heß S., Springel V., 2010, *MNRAS*, 406, 2289
- Iapichino L., Niemeyer J. C., 2008, *MNRAS*, 388, 1089
- Iapichino L., Schmidt W., Niemeyer J. C., Merklein J., 2011, *MNRAS*, 414, 2297
- Jones T. W., Porter D. H., Ryu D., Cho J., 2011, *Mem. Soc. Astron. Italiana*, 82, 588
- Keres D., Vogelsberger M., Sijacki D., Springel V., Hernquist L., 2011, *ArXiv e-prints*, 1109.4638
- Kitsionas S., Federrath C., Klessen R. S., Schmidt W., Price D. J., Dursi L. J., Gritschneider M., Walch S., Piontek R., Kim J., Jappsen A.-K., Ciecielag P., Mac Low M.-M., 2009, *A&A*, 508, 541
- Klessen R. S., Heitsch F., Mac Low M.-M., 2000, *ApJ*, 535, 887
- Kritsuk A. G., Nordlund Å., Collins D., Padoan P., Norman M. L., Abel T., Banerjee R., Federrath C., Flock M., Lee D., Li P. S., Müller W.-C., Teyssier R., Ustyugov S. D., Vogel C., Xu H., 2011, *ApJ*, 737, 13
- Lau E. T., Kravtsov A. V., Nagai D., 2009, *ApJ*, 705, 1129
- Mac Low M.-M., Klessen R. S., 2004, *Reviews of Modern Physics*, 76, 125
- Mac Low M.-M., Klessen R. S., Burkert A., Smith M. D., 1998, *Physical Review Letters*, 80, 2754
- Maier A., Iapichino L., Schmidt W., Niemeyer J. C., 2009, *ApJ*, 707, 40
- Meyers J., Meneveau C., 2008, *Physics of Fluids*, 20, 065109
- Mitchell N. L., McCarthy I. G., Bower R. G., Theuns T., Crain R. A., 2009, *MNRAS*, 395, 180
- Monaghan J. J., 1997, *J. Comp. Phys.*, 136, 298
- Monaghan J. J., 2011, *European Journal of Mechanics B Fluids*, 30, 360
- Morris J., 1997, *Journal of Computational Physics*, 136, 41
- Muñoz D., Springel V., Marcus R., Vogelsberger M., Hernquist L., 2012, *ArXiv e-prints*, 1203.1037
- Padoan P., Nordlund Å., Kritsuk A. G., Norman M. L., Li P. S., 2007, *ApJ*, 661, 972
- Pakmor R., Bauer A., Springel V., 2011, *MNRAS*, 418, 1392
- Parrish I. J., McCourt M., Quataert E., Sharma P., 2012, *MNRAS*,

- 419, L29
- Paul S., Iapichino L., Miniati F., Bagchi J., Mannheim K., 2011, *ApJ*, 726, 17
- Petkova M., Springel V., 2011, *MNRAS*, 415, 3731
- Pope S. B., 2000, *Turbulent Flows*. Cambridge University Press
- Price D. J., 2008, *Journal of Computational Physics*, 227, 10040
- Price D. J., 2012, *MNRAS*, 420, L33
- Price D. J., Federrath C., 2010, *MNRAS*, 406, 1659
- Quinlan N. J., Basa M., Lastiwka M., 2006, *International Journal for Numerical Methods in Engineering*, 66, 2064
- Rasio F. A., 2000, *Progress of Theoretical Physics Supplement*, 138, 609
- Read J. I., Hayfield T., 2011, *ArXiv e-prints*, 1111.6985
- Read J. I., Hayfield T., Agertz O., 2010, *MNRAS*, 405, 1513
- Robinson M., Monaghan J. J., 2011, *ArXiv e-prints*, 1101.2240
- Rosswog S., 2009, *New A Rev.*, 53, 78
- Ryu D., Kang H., Cho J., Das S., 2008, *Science*, 320, 909
- Schmidt W., Federrath C., 2011, *A&A*, 528, A106
- Schmidt W., Hillebrandt W., Niemeyer J. C., 2006, *Computers & Fluids*, 35, 353
- Schuecker P., Finoguenov A., Miniati F., Böhringer H., Briel U. G., 2004, *A&A*, 426, 387
- Sijacki D., Springel V., 2006, *MNRAS*, 371, 1025
- Sijacki D., Vogelsberger M., Keres D., Springel V., Hernquist L., 2011, *ArXiv e-prints*, 1109.3468
- Springel V., 2005, *MNRAS*, 364, 1105
- Springel V., 2010, *MNRAS*, 401, 791
- Springel V., 2010, *ARA&A*, 48, 391
- Springel V., Hernquist L., 2002, *MNRAS*, 333, 649
- Subramanian K., Shukurov A., Haugen N. E. L., 2006, *MNRAS*, 366, 1437
- Valdarnini R., 2011, *A&A*, 526, A158
- Vazza F., Brunetti G., Gheller C., Brunino R., Brüggem M., 2011, *A&A*, 529, A17
- Vazza F., Brunetti G., Kritsuk A., Wagner R., Gheller C., Norman M., 2009, *A&A*, 504, 33
- Vazza F., Tormen G., Cassano R., Brunetti G., Dolag K., 2006, *MNRAS*, 369, L14
- Viola D., Issa R., 2007, *International Journal for Numerical Methods in Fluids*, 53, 277
- Vogelsberger M., Sijacki D., Keres D., Springel V., Hernquist L., 2011, *ArXiv e-prints*, 1109.1281
- Wadsley J. W., Veeravalli G., Couchman H. M. P., 2008, *MNRAS*, 387, 427
- Zhu W., Feng L.-l., Fang L.-Z., 2010, *ApJ*, 712, 1
- Zhu W., Feng L.-L., Fang L.-Z., 2011, *MNRAS*, 415, 1093
- ZuHone J. A., 2011, *ApJ*, 728, 54